



LEONARDO ALMEIDA DE SÁ

Anisotropia do manto superior na intraplaca sulamericana.

Nº da dissertação: 527

Brasília - DF

July/2024



LEONARDO ALMEIDA DE SÁ

**ANISOTROPIA DO MANTO SUPERIOR NA INTRAPLACA SULAMERICANA.
Nº DA DISSERTAÇÃO: 527**

Master's dissertation submitted to the Coordination of the Graduate Program in Geology at the University of Brasília to obtain the Master's degree in Geology.

Adiviser: Prof. Dr. George Sand Leão Araújo de França

Brasília - DF

July/2024

Leonardo Almeida de Sá

Anisotropia do manto superior na intraplaca sulamericana.

Nº da dissertação: 527/ Leonardo Almeida de Sá. – Brasília - DF, July/2024-
59 p. : il. (algumas color.) ; 30 cm.

Adiviser: Prof. Dr. George Sand Leão Araújo de França

Master's dissertation – University of Brasilia – UnB

Campus Darcy Ribeiro

Master's Degree Geology, July/2024.

1. Anisotropy. 2. Shear Wave Splitting. 2. Amazonian Craton. 3. Database. I. Adiviser. II. University of Brasilia. III. Campus Darcy Ribeiro. IV. Mantle anisotropy around the Amazonian craton and database: Anisotropy of the upper mantle in Brazil and asthenospheric flow around the Amazonian craton.

LEONARDO ALMEIDA DE SÁ

**ANISOTROPIA DO MANTO SUPERIOR NA INTRAPLACA SULAMERICANA.
Nº DA DISSERTAÇÃO: 527**

Brasília - DF, July 12, 2024:

Prof. Dr. George Sand Leão Araújo de França.
Adiviser
University of São Paulo

*This work is dedicated to my mother, who always taught me
that everything that is started must be finished.*

ACKNOWLEDGEMENTS

May all honor and glory be given to the Lord Jesus Christ, without whom none of this work would have been possible. I would like to thank Professor George Sand (USP) for his immense contribution to my academic life and for allowing me to enter the master's program; I am eternally grateful. I also thank my mother, Vanja Suely, for her immense encouragement and love during my studies, guiding me and showing me that the path of study is the path of light. This study was financed in part by the Coordenação de Aperfeiçoamento de Pessoal de Nível Superior - Brazil (CAPES) - Finance Code 001. Figures were prepared using the Generic Mapping Tools (GMT) software package ([Wessel et al., 2019](#)). I extend my sincere gratitude to Professor Carlos Magno, Aline Montenegro, and Professor George França of the University of São Paulo for their invaluable support and guidance throughout the completion of this dissertation. Their expertise, encouragement, and steadfast assistance have played a pivotal role in shaping this work. I am profoundly grateful for their dedication and commitment to my academic endeavors.

*“Não vos amoldeis às estruturas deste mundo,
mas transformai-vos pela renovação da mente,
a fim de distinguir qual é a vontade de Deus:
o que é bom, o que Lhe é agradável, o que é perfeito.
(Bíblia Sagrada, Romanos 12, 2)*

RESUMO

A anisotropia sísmica investiga como as ondas sísmicas mudam dependendo da direção ao interagir com diferentes materiais do manto superior. Este estudo foca na anisotropia do manto superior na intraplaca da América do Sul, especialmente em relação aos padrões de fluxo da astenosfera ao redor do cráton amazônico. Utilizando técnicas avançadas de análise sísmica e dados regionais, a pesquisa busca revelar a relação entre estruturas geológicas e propriedades das ondas sísmicas, mostrando uma correlação entre a anisotropia do manto superior e o movimento absoluto da placa, além de associações com estruturas geológicas, como a colisão do Cráton São Francisco com o micro-contidente Paraná durante a acreção brasileira. A olivina, mineral predominante no manto (65%vol.), desenvolve uma Orientação Preferencial Cristalográfica (CPO) sob força cisalhante, correlacionando sua orientação com direções de fluxo do manto. A análise de variações nas ondas primárias no Moho (Hess et al., 1964) destaca o potencial da divisão das ondas de cisalhamento para investigar eventos passados e visualizar padrões de fluxo astenosférico. Dados da Universidade de São Paulo (USP) e da Rede Sismográfica Brasileira (RSBR) incluíram 72 estações e mais de 1700 pontos de dados de divisão de ondas de cisalhamento, fornecendo novos parâmetros e atualizando mapas anteriores. No cráton amazônico, os valores médios de direção de polarização rápida (ϕ) e tempo de atraso (δt) foram $90,23 \pm 10,78$ e $0,76 \pm 0,15$, respectivamente; no cráton do São Francisco, $109,17 \pm 14,25$ e $0,67 \pm 0,16$; na bacia do Paraná, $84,52 \pm 12,23$ e $0,88 \pm 0,23$; no Cinturão de Dobramentos Ribeira, $85,26 \pm 6,89$ e $1,02 \pm 0,4$; na Província Tocantins, $89,33 \pm 1,95$ e $1,28 \pm 0,09$; na Bacia do Chaco-Paraná, $102,45 \pm 12,59$ e $0,97 \pm 0,19$; e na Bacia do Paranaíba, $94,62 \pm 18,17$ e $0,71 \pm 0,35$. As direções de polarização rápida na bacia amazônica geralmente seguem o movimento absoluto da placa (APM) em ENE-OSO, com deflexões perto da raiz cratônica do Brasil Central, sugerindo influência do fluxo astenosférico. A Bacia do Chaco-Paraná reflete a influência do bloco Paranapanema. Em termos de tempo de atraso, os cinturões de dobramentos apresentam valores mais altos que os crátons, possivelmente devido ao ciclo de acreção brasileiro criando uma grande camada anisotrópica. As direções de polarização rápida correlacionam-se com o movimento absoluto da placa em ENE-OSO, com exceções no Cráton São Francisco e na Província do Tocantins, influenciadas pelo fluxo astenosférico que contorna a raiz do Cráton São Francisco.

Palavras-chave: Anisotropia; Manto Superior; Cratons; Divisão de ondas cisalhantes.

ABSTRACT

Seismic anisotropy investigates how seismic waves change depending on the direction when interacting with different materials in the upper mantle. This study focuses on upper mantle anisotropy in the intraplate region of South America, particularly concerning asthenospheric flow patterns around the Amazonian craton. Utilizing advanced seismic analysis techniques and regional data, the research aims to reveal the relationship between geological structures and seismic wave properties, demonstrating a correlation between upper mantle anisotropy and absolute plate motion, along with associations with geological structures such as the collision of the São Francisco Craton with the Paraná microcontinent during the Brasiliano accretion. Olivine, the predominant mineral in the mantle (65%vol.), develops a Crystallographic Preferred Orientation (CPO) under shear stress, correlating its orientation with mantle flow directions. The analysis of variations in primary waves at the Moho (Hess et al., 1964) highlights the potential of shear wave splitting to investigate past events and visualize asthenospheric flow patterns. Data from the University of São Paulo (USP) and the Brazilian Seismographic Network (RSBR) included 72 stations and over 1700 shear wave splitting data points, providing new parameters and updating previous maps. In the Amazonian craton, the study found average values of fast polarization direction (ϕ) and delay time (δt) to be 90.23 ± 10.78 degrees and 0.76 ± 0.15 seconds, respectively; in the São Francisco craton, 109.17 ± 14.25 degrees and 0.67 ± 0.16 seconds; in the Paraná Basin, 84.52 ± 12.23 degrees and 0.88 ± 0.23 seconds; in the Ribeira Fold Belt, 85.26 ± 6.89 degrees and 1.02 ± 0.4 seconds; in the Tocantins Province, 89.33 ± 1.95 degrees and 1.28 ± 0.09 seconds; in the Chaco-Paraná Basin, 102.45 ± 12.59 degrees and 0.97 ± 0.19 seconds; and in the Parnaíba Basin, 94.62 ± 18.17 degrees and 0.71 ± 0.35 seconds. Fast polarization directions in the Amazonian Basin generally follow the absolute plate motion in an ENE-WSW direction, with deflections near the cratonic root of Central Brazil, suggesting the influence of asthenospheric flow. The Chaco-Paraná Basin reflects the influence of the Paranapanema block. In terms of delay time, the fold belts exhibit higher values than the cratons, possibly due to the Brasiliano accretion cycle creating a large anisotropic layer. The fast polarization directions correlate with the absolute plate motion in an ENE-WSW direction, with exceptions in the São Francisco Craton and Tocantins Province, influenced by asthenospheric flow.

Keywords: Anisotropy; Upper Mantle; Cratons; Shear Wave Splitting.

LIST OF FIGURES

Figure 1 – Graphical representation of birefringence in calcite.	13
Figure 2 – Comparative graphs of ϕ (Phi) and Δt (Dt) values for each station, between data from Melo et al. (2018) and those obtained for this study. Error bars were calculated as the difference between data from Melo et al. (2018) and those of these studies.	34
Figure 3 – Averages of polarization directions and their respective errors for each province in South America. a) The orange bars represent the average values for the cratons, the pale yellow bars correspond to the values presented by the fold belts, and the blue bars refer to the basins. b) The average values of fast polarization direction obtained in the Amazonian craton were derived from 12 stations in the region, while in the São Francisco craton, there were 5 stations. c) In the Tocantins fold belt, data were obtained from 2 stations, and in the Ribeira fold belt, from 4 stations. d) For the Amazon basin, the data came from 7 stations, the Parnaíba basin had 3 stations, the Paraná basin had data from 22 stations, and the Chaco-Paraná basin had data from 6 stations. SFC is San Francisco Craton, we used as reference (Cordani et al., 2016)	35
Figure 4 – Averages of delay time and their respective errors for each province in South America. a) The orange bars represent the average values for the cratons, the pale yellow bars correspond to the values presented by the fold belts, and the blue bars refer to the basins. b) The average values of fast polarization direction obtained in the Amazonian craton were derived from 12 stations in the region, while in the São Francisco craton, there were 5 stations. c) In the Tocantins fold belt, data were obtained from 2 stations, and in the Ribeira fold belt, from 4 stations. d) For the Amazon basin, the data came from 7 stations, the Parnaíba basin had 3 stations, the Paraná basin had data from 22 stations, and the Chaco-Paraná basin had data from 6 stations. SFC is San Francisco Craton, we used as reference as (Cordani et al., 2016)	36
Figure 5 – SplitWave Application Homepage: The application already includes the data presented in this study.	37
Figure 6 – Data Viewing Page: Users can search for data by station name in the white search tab on the right. To search by author, the white search tab on the left is available. To view a complete list of the studies used, users can click on the orange tab. Additionally, the page allows for the viewing of a map, which displays the location of the data. By clicking on each marker on the map, corresponding information for each station will be displayed.	38
Figure A.1– Anisotropic parameters obtained through the bootstrap technique at station AQDB, displaying the distribution of observed values (blue bars), the normal distribution curve (orange line), and the estimated value for the parameters (dashed orange vertical line).	45
Figure A.2– Anisotropic parameters obtained through the bootstrap technique at station BEB11, displaying the distribution of observed values (blue bars), the normal distribution curve (orange line), and the estimated value for the parameters (dashed orange vertical line).	45
Figure A.3– Anisotropic parameters obtained through the bootstrap technique at station BOAV, displaying the distribution of observed values (blue bars), the normal distribution curve (orange line), and the estimated value for the parameters (dashed orange vertical line).	46

Figure A.19–Anisotropic parameters obtained through the bootstrap technique at station PRPB, displaying the distribution of observed values (blue bars), the normal distribution curve (orange line), and the estimated value for the parameters (dashed orange vertical line).	54
Figure A.20–Anisotropic parameters obtained through the bootstrap technique at station PTLB, displaying the distribution of observed values (blue bars), the normal distribution curve (orange line), and the estimated value for the parameters (dashed orange vertical line).	54
Figure A.21–Anisotropic parameters obtained through the bootstrap technique at station ROIB, displaying the distribution of observed values (blue bars), the normal distribution curve (orange line), and the estimated value for the parameters (dashed orange vertical line).	55
Figure A.22–Anisotropic parameters obtained through the bootstrap technique at station ROSB, displaying the distribution of observed values (blue bars), the normal distribution curve (orange line), and the estimated value for the parameters (dashed orange vertical line).	55
Figure A.23–Anisotropic parameters obtained through the bootstrap technique at station SDBA, displaying the distribution of observed values (blue bars), the normal distribution curve (orange line), and the estimated value for the parameters (dashed orange vertical line).	56
Figure A.24–Anisotropic parameters obtained through the bootstrap technique at station SICB, displaying the distribution of observed values (blue bars), the normal distribution curve (orange line), and the estimated value for the parameters (dashed orange vertical line).	56
Figure A.25–Anisotropic parameters obtained through the bootstrap technique at station SJMB, displaying the distribution of observed values (blue bars), the normal distribution curve (orange line), and the estimated value for the parameters (dashed orange vertical line).	57
Figure A.26–Anisotropic parameters obtained through the bootstrap technique at station TBTG, displaying the distribution of observed values (blue bars), the normal distribution curve (orange line), and the estimated value for the parameters (dashed orange vertical line).	57
Figure A.27–Anisotropic parameters obtained through the bootstrap technique at station TRIB, displaying the distribution of observed values (blue bars), the normal distribution curve (orange line), and the estimated value for the parameters (dashed orange vertical line).	58
Figure A.28–Anisotropic parameters obtained through the bootstrap technique at station VABB, displaying the distribution of observed values (blue bars), the normal distribution curve (orange line), and the estimated value for the parameters (dashed orange vertical line).	58
Figure A.29–Anisotropic parameters obtained through the bootstrap technique at station VILB, displaying the distribution of observed values (blue bars), the normal distribution curve (orange line), and the estimated value for the parameters (dashed orange vertical line).	59

CONTENTS

1	INTRODUCTION	13
1.0.1	Organization of the thesis	13
1.0.2	Olivine: A Mineral of Great Importance for the Anisotropic Study of the Mantle	13
2	METHODOLOGY	16
2.1	Minimum Energy Method	16
2.2	Misorientation of Station	17
2.3	Grid Search	17
2.4	<i>bootstrap</i> statistical calculation	18
3	ANISOTROPY OF THE UPPER MANTLE IN BRAZIL AND ASTHENOSPHERIC FLOW AROUND THE AMAZONIAN CRATON	19
4	RESULTS AND DISCUSSION	33
4.1	Analysis of Direction of Polarization (ϕ) and Delay time (Δt) Values	34
5	TECHNOLOGIES USED IN THE DEVELOPMENT OF THE SPLITWAVE FRAMEWORK	37
5.1	Back-end: Technologies and Operation	37
5.1.1	Node.js	37
5.1.2	Hono	37
5.1.3	Prisma	37
5.1.4	PostgreSQL	38
5.2	Front-end: Technologies and Architecture	38
5.2.1	Astro	38
5.2.2	Front-end and Back-end Integration	38
5.3	Hosting and Infrastructure	39
5.3.1	Vercel and Google Cloud Run	39
5.3.2	PostgreSQL Database on Amazon Web Services	39
6	CONCLUSIONS	40
	BIBLIOGRAPHY	42
	APPENDIX	44
	APPENDIX A – BOOSTRAPPING	45

1 INTRODUCTION

1.0.1 Organization of the thesis

This master's dissertation is organized into 6 chapters. Chapter one provides an overview of the study's structure, objectives, seismic anisotropy behavior in the upper mantle, and the behavior and properties of Olivine in the mantle. Chapter two offers a detailed description of the methodology employed in this study, with the calculations from [Silver \(1996\)](#) appropriately corrected. Chapter three consists of a paper submitted to the *Journal of South American Earth Sciences* and is currently under review for publication. In this chapter presents a discussion and enhanced description of the obtained parameters and behavior within the provinces present in Brazil. Chapter four presents the results and discussions derived from the analysis of the results. Considering that this is covered in more detail in the paper, the emphasis is on presenting the overall framework. Chapter five details the SplitWave database ([Sá et al., 2024](#)), its functioning, and its technologies. Finally, chapter six concludes the study.

Anisotropy within the Earth occurs similarly to the phenomenon optic called birefringence, which involves the polarization of light when interacting with a medium. For example, light undergoes a filtering process, thereby dividing and providing distinct phenomena. In [Figure 1](#), calcite acts as a filter due to its orthorhombic cleavage, serving as an example that demonstrates the visualization of light birefringence; when placed over an object, a duplicated image can be observed. This occurs because light divides (polarizes) along orthogonal directions, meaning that light propagates more rapidly along one axis than along another. In the case of seismic anisotropy, an elliptical particle motion is observed, whereas the ideal motion of wave interaction with a body is linear.



Figure 1 – Graphical representation of birefringence in calcite.

1.0.2 Olivine: A Mineral of Great Importance for the Anisotropic Study of the Mantle

Olivine, a mineral of significant importance in the study of mantle anisotropy, is the most abundant component of the Earth's upper mantle, making up approximately 60% of its volume. This mineral belongs to the category of nesosilicates and is commonly found in igneous rocks. It is characterized by an orthorhombic bipyramidal crystal system, with its green color being one of its distinctive features.

The deformability of Olivine is a crucial factor in the anisotropy of the upper mantle, resulting from the splitting of shear waves. Therefore, it is important to emphasize that the deeper our understanding of Olivine's behavior, the more precise our analyses will be regarding the XK(K)S wave splitting ([Demouchy; Wang; Tommasi, 2023](#)). From this point forward, the notation XK(K)S will be used to encompass all seismic phases that interact with the core-mantle boundary. These include SKS, SKKS, and PKS phases.

According to [Abramson et al. \(1997\)](#), Olivine exhibits strong elastic anisotropy. Moreover, its preferred axes can be altered according to the environmental conditions in which it is found. A study conducted by [Demouchy, Wang and Tommasi \(2023\)](#) analyzed over 700 samples of naturally deformed peridotites, concluding that 95% of the samples exhibited a preferential crystal orientation along the [100] axis (Axis A), which corresponds to being parallel to the flow direction. This phenomenon occurs because Olivine is present in a medium characterized by high temperatures, moderate pressure, and a low percentage of water. Under these conditions, the mineral is influenced by a shearing region, as mentioned by [Bystricky et al. \(2000\)](#).

The crystallographic preferred orientation (CPO) of Olivine creates a relationship between flow geometry and seismic anisotropy orientation. This relationship enables the determination of fast S-wave polarization directions and the inference of asthenospheric flow direction based on the propagation of P and Rayleigh waves. However, the relationship between flow geometry and observed seismic anisotropy will exhibit significant differences depending on the region of the mantle in which Olivine is located ([Demouchy; Wang; Tommasi, 2023](#)).

In shear zones in the asthenosphere, Olivine behaves as described above. However, in subduction zones where there is high pressure, hydration, and continuous stress, there is a shift in the preferred axis of Olivine. In these cases, the [001] axis is favored over the [100] axis. [Andrade and Assumpção \(2008\)](#) reported this effect in the 2000s, although at the time, he did not know what was causing the variation in the direction of anisotropy in the Andean region. However, in his dissertation, [Andrade \(2008\)](#) raised questions and pointed out possible reasons that could explain the different polarization directions.

Several researchers have advanced hypotheses to elucidate this phenomenon. Notably, [Silver and Chan \(1991\)](#) posited that the preferred orientation of the mantle at lithospheric depths, induced by strike-slip movements and associated with vertical shear zones, could explain why the directions of maximum anisotropy align parallel to mountain belts. Conversely, [Nicolas \(1993\)](#) contended that vertical shear zones alone cannot account for this phenomenon, as lithospheric shear zones generally do not exceed 100 km in width, whereas directions of fast polarization are observed parallel to the mountain belt extending up to 200 km in thickness. This discrepancy indicates that additional factors besides strike-slip movements might influence the observed anisotropy at greater depths.

Another possible explanation was presented by [Russo and Silver \(1994\)](#) and [Anderson \(1961\)](#) that proposed that the directions of maximum polarization, being parallel to the Andean chain, would result from asthenospheric flow laterally deflecting due to the subduction zone. The latter, in turn, would be functioning as a kind of barrier. This study, like the previous ones, brings important contributions to understanding Olivine's behavior and its implications in mantle anisotropy. To deeply understand Olivine's behavior, it is necessary to adopt a microscopic perspective to examine what may be happening in the background. Olivine exhibits various deformation patterns, all directly dependent on the environmental conditions in which it is found.

According [Demouchy, Wang and Tommasi \(2023\)](#), Olivine has three main mechanisms of ductile deformation: diffusion, dislocation, and mechanisms related to grain boundaries. Each of these mechanisms presents distinct characteristics that contribute to understanding Olivine's behavior under different conditions.

In diffusion deformation, the grain tends to decrease in relation to the direction of maximum compression, while elongating in the direction of minimum compression. This phenomenon suggests a dynamic capacity of Olivine to adapt and reconfigure in response to external forces.

On the other hand, dislocation deformations occur due to translational linear movement through

the crystal lattice. This type of deformation is characterized by the combination of slip directions and slip planes, resulting in what is called the crystal's slip system. A notable characteristic of Olivine is that it has only three independent slip systems. This limitation causes a rotation of the grains of a crystallographic lattice, producing the mineral's preferred orientation (CPO). This process gradually aligns the slip system with the direction of mantle flow, as documented by [Demouchy, Wang and Tommasi \(2023\)](#).

These mechanisms of Olivine deformation, which occur on a microscopic scale, have significant implications for understanding Olivine's behavior on a macroscopic scale. The observation and analysis of these mechanisms can provide valuable insights into mantle anisotropy and Earth dynamics.

2 METHODOLOGY

The phases primarily used were SKS phases, which have a relatively broad propagation radius, corresponding to an epicentral window from 85° to 130°. Additionally, the SKS phase travels a longer path, reaching great depths, as it travels from the seismic wave source to the outer core and then reflects back to the receiver, carrying information about subsurface physical parameters.

Among the various techniques developed over the years to analyze seismic phases and obtain estimates of fast polarization direction and delay time, the ones used in this study were developed by [Silver and Chan \(1991\)](#), sensor misorientation, and grid averaging of the energy reduction of the transverse component along with statistical bootstrap calculations for error estimates. XK(K)S phases were chosen due to their nearly vertical incidence; thus, the anisotropy is situated below the station. When interacting with the core-mantle boundary, the waves undergo conversion along with polarization of the P-wave (which is almost parallel to the wave propagation direction) and the S-wave (radial polarization in SV and SH). The particle motion should be linear, considering the vertical incidence; however, with the phase delay of about 1.0 second, an elliptical motion is observed instead of two separate waves.

For the data analysis, the MATLAB-based software SplitRacer was employed ([Reiss; Rumpker, 2017](#)). SplitRacer is a MATLAB graphical interface specifically designed to handle large datasets efficiently. It features a combination of automated processes and user-managed functions, allowing for dynamic involvement in the data analysis workflow.

The software provides an array of functionalities designed to ensure precise measurements and comprehensive analyses, all while adhering to quality parameters set by the user. Data can be conveniently downloaded directly through the interface and are immediately available for use after segmentation into a three-component, one-hour seismogram format.

2.1 Minimum Energy Method

When shear seismic waves interact with an anisotropic medium and undergo wave splitting, they carry a considerable amount of energy in the transverse component, while the vertical component remains crucial and predominant for studies. It is essential to drastically reduce the energy present in the direction of the transverse axis. To achieve this, the minimum energy method formulated and developed by [Silver and Chan \(1991\)](#) is employed. The method consists of:

Assuming that, for all frequencies ω , the displacement $\mu(t, X|\omega)$ caused by a wave at a distance "X" from the source and at time "t" is parallel to a simple polarization vector \vec{p} .

$$\mu(t, X|\omega, k) = A(\omega) \cdot \exp(-i \cdot \omega \cdot T_0) \cdot \vec{p}, \quad (2.1)$$

where $A(\omega) = \omega(\omega)\hat{A}(\omega)$ is the complex vector amplitude, T_0 is the time at which the wave arrives at the surface, $k(\omega)$ is the wave number and to find the total displacement of the wave, the integral is carried out in function of ω of the polarization vector with the limits going from 0 to infinity Equation 2.2, resulting in Equation 2.3

$$\mu(t, x) = \int_0^\infty \mu(t, X|\omega, k(\omega))d\omega, \quad (2.2)$$

$$\mu(t, \omega) = w(\omega) \cdot e^{-i\omega t} \cdot \vec{p}, \quad (2.3)$$

In Equation 2.3, the $w(\omega)$ is the norm of amplitude with angular frequency ω , the dependence on the distance X was removed, assuming that the displacement is being observed at a single seismograph on the Earth's surface. When the wave reaches the surface, there is a component that travels more rapidly, known as the fast polarization (\vec{f}), while with a time difference (δt), the direction of slow polarization (\vec{s}) arrives later at the surface. The displacement of the split wave can be represented by a division operator:

$$\Gamma(\phi, \delta t; \omega) = e^{-i\omega\delta t/2} \vec{f}\vec{f}^T + e^{+i\omega\delta t/2} \vec{s}\vec{s}^T + \vec{b}\vec{b}^T = e^{-i\omega\delta T(\phi, \delta t)}, \quad (2.4)$$

Performing a comparison between the division operator presented by Walsh, Arnold and Savage (2013) and that of Silver and Chan (1991), it is observed that the signals are opposite, ensuring that the slower pulse remains behind the fast polarization component.

Furthermore, in Equation 2.4, the presence of a time difference tensor is observed, defined as:

$$\delta T(\phi, \delta t, \omega) = (\delta t/2) \cdot (\vec{f}\vec{f}^T - \vec{s}\vec{s}^T) \quad (2.5)$$

The tensor allows the division operator to be written in a reduced form, dependent on division parameters, namely the delay time (δt) and polarization direction (ϕ).

In a simplified manner, the division operator is applied to Equation 2.1 to obtain an equation for the split wave, represented by:

$$\mu_s(\omega) = W(\omega) \cdot e^{(-i\omega T_0)} \cdot \Gamma(\phi, \delta t) \cdot \vec{p} \quad (2.6)$$

Subsequently, an appropriate pair of parameters (delay time and fast polarization direction) must be found, returning Equation 2.6 to Equation 2.1 using an inverse division operator Γ^{-1} . In summary, the minimum energy and eigenvalue method aim to find parameters through a grid search that can be inserted into Equation 2.6 and return to Equation 2.1. By doing so, the energy in the transverse component is minimized, and the particle motion is linearized.

2.2 Misorientation of Station

During the pre-processing stages of SK(K)S phases in SplitRacer, developed by Reiss and Rümper (2017), an analysis of sensor misorientation at a station is conducted based on the seismic phases that were visualized and saved in the visual quality check section. Over the years, it is common for the sensor orientation value to change, and these changes can be detected. If the program-calculated average misorientation exhibits significant dispersion across all data, it becomes necessary to consider the possibility of using the misorientation provided by each phase instead of relying on the station's average misorientation value. Regardless, the information will be saved so that the user can decide later which option to apply in the data processing.

2.3 Grid Search

The SplitRacer program calculates a grid of reduced average energy over all selected time windows (default is 50 time intervals selected around the phase), with a confidence level of 95%. The code lines

for this task are based on those used by [Wüstefeld et al. \(2008\)](#) during the development of the SplitLab software, which also aims to assist in the analysis of shear wave splitting.

The grid search is grounded in error estimation calculations developed by [Silver and Chan \(1991\)](#). It is assumed that the signal is combined with Gaussian white noise, where the energy of the transverse component is a random variable, with "n" degrees of freedom, used in the fast polarization direction and delay time test. However, [Walsh, Arnold and Savage \(2013\)](#) identified the presence of derivative errors in the calculations presented by [Silver and Chan \(1991\)](#), resulting in an overestimation of degrees of freedom and providing analyses with smaller errors.

In an attempt to remedy the underestimation of errors, ([Reiss; Rämpker, 2017](#)) derived the splitting parameters obtained for the minimum 95% confidence level. After obtaining these parameters, they are applied in the inverse division operator, which demonstrated greater efficiency in reducing energy in the transverse component.

2.4 *bootstrap* statistical calculation

Developed by [Efron \(1979\)](#), bootstrap is a statistical method aimed at visualizing the distributional characteristics of a random variable. Typically, this technique is employed when the distribution under analysis presents complex analytical evaluation. Originating from English, the term "bootstrap" is derived from the expression "to pull oneself up by one's bootstraps," which can be freely translated as "lifting oneself up by pulling on one's own shoelaces." In statistical context, this phrase is used to illustrate that it is possible to obtain properties of large samples through a few observations.

Operationally, the bootstrap technique performs sampling with replacement, where the sample size equals that of the original sample. "X" draws are conducted, where "X" represents the size of the original sample, resulting in a bootstrap sample. This operation is repeated "n" times, generating "n" bootstrap samples. With these samples, it is possible to construct a distribution curve of the desired variable. [Efron \(1979\)](#) found that the bootstrap distribution tends to approach the true distribution as the number of bootstrap samples tends to infinity. Based on this information, [Link, Reiss and Rämpker \(2022\)](#) adopted this statistical technique to obtain a better estimate of errors for wave splitting, assuming a single layer.

3 ANISOTROPY OF THE UPPER MANTLE IN BRAZIL AND ASTHENOSPHERIC FLOW AROUND THE AMAZONIAN CRATON



Anisotropy of The Upper Mantle South American Intraplate

Leonardo Almeida de Sá^{a,1,*}, Aline Montenegro^b, Carlos A. M. Chaves^b, George Sand França^b

^a*Observatório Sismológico, Instituto de Goeciências, Universidade de Brasília, Brasília 70.910-900, Brasil*

^b*Centro de Sismologia, Instituto de Astronomia, Geofísica e Ciências Atmosféricas, Universidade de São Paulo, São Paulo 05508-090, Brazil*

Abstract

A seismic anisotropy study is an investigation into how physical properties changes depending on the direction in which it interacts with a body. In the upper mantle, this concept relates to how seismic wave propagation speeds vary when interacting with different materials. This particular study focuses on understanding upper mantle anisotropy in the South America plate, particularly in relation to the asthenospheric flow around the Amazonian craton. By employing advanced seismic analysis techniques and utilizing regional data, the study aims to uncover the relationship between geological structures and seismic wave properties. The findings reveal a significant correlation between upper mantle anisotropy and asthenospheric flow patterns. In the Amazonian craton, this work found average values of fast polarization direction (ϕ) and Delay Time (δt) to be $90.23^\circ \pm 10.78^\circ$ and $0.76 \text{ s} \pm 0.15 \text{ s}$, respectively. For the São Francisco craton, these values were $109.17^\circ \pm 14.25^\circ$ and $0.67 \text{ s} \pm 0.16 \text{ s}$. In the Paraná Basin, the values were ϕ of $84.52^\circ \pm 12.23^\circ$ and δt of $0.88 \text{ s} \pm 0.23 \text{ s}$, while the Ribeira Fold Belt presented values of ϕ of $85.26^\circ \pm 6.89^\circ$ and δt of $1.02 \text{ s} \pm 0.4 \text{ s}$. The Tocantins Province showed values of ϕ of $89.33^\circ \pm 1.95^\circ$ and δt of $1.28 \text{ s} \pm 0.09 \text{ s}$. The Chaco-Paraná Basin exhibited ϕ of $102.45^\circ \pm 12.59^\circ$ and δt of $0.97 \text{ s} \pm 0.19 \text{ s}$, and the Paranaíba Basin had ϕ of $94.62^\circ \pm 18.17^\circ$ and δt of $0.71 \text{ s} \pm 0.35 \text{ s}$. Visualization of variations in primary waves at the Moho (Hess et. al, 1964) demonstrated that the analysis of shear wave splitting has significant potential for investigating past events and visualizing current asthenospheric flow patterns. The data for this study were obtained from the University of São Paulo (USP) network through the FDSN request, with stations available in the Brazilian Seismographic Network (RSBR). A total of 72 stations and over 1700 Shear wave splitting data were analyzed, providing new parameters for seismic anisotropy studies and updated previous maps. The results indicate that the stable South American plate exhibits fast polarization in the East to NNW-SSE direction, while the cratons maintain a more NNW-SSE orientation. The Chaco-Paraná Basin reflects the influence of the stable part of the basin. In terms of delay time, fold belts exhibit higher values compared to cratons, which have lower values.

Keywords: Seismic anisotropy, Upper mantle, Asthenospheric flow, Amazonian craton and Geological evolution.

1. Introduction

Through the visualization of variations in primary waves at the Moho, [18] pioneered studies on anisotropy. His research revealed that shear wave splitting analysis held significant potential as an effective tool for probing past events and visualizing current patterns of asthenospheric flow.

By observing the rocks present in the crust, we can ascertain the evolutionary history and tectonic processes that have occurred over many years and their outcomes. Seismic anisotropy allows us to visualize these evolutionary and orogenic processes through the patterns of minerals present in the upper mantle, referred to as frozen and/or

*Corresponding author. Observatório Sismológico, Instituto de Goeciências, Universidade de Brasília, Brasília 70.910-900, Brasil
E-mail address: 220003645@aluno.unb.br

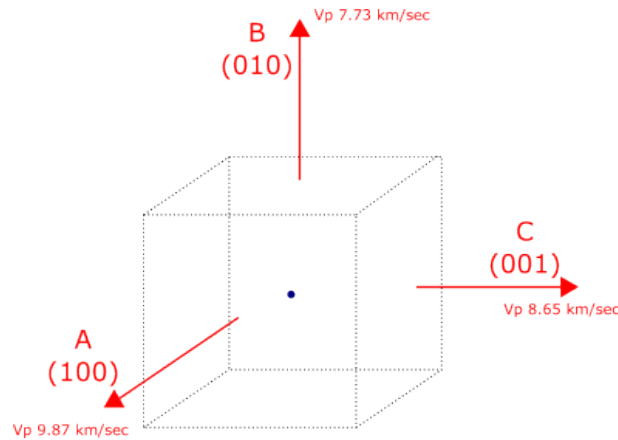


Figure 1. Preferential orientation of the optical axes, speed values for the p wave (V_p) when interacting with each axis. Adapted from Hess [18].

fossilized anisotropy. Fossilized anisotropy results from the influence of asthenospheric flow on minerals, generating a preferential mineral orientation that becomes fossilized, providing information about the past tectonic processes to which the minerals were subjected.

The physical definition of anisotropy is the ability of a physical property to vary according to a direction when interacting with a body. Seismic anisotropy concerns the variation in wave propagation velocity when interacting with a material. According to [22], when a shear wave interacts with an anisotropic medium, it is split into two mutually orthogonal pulses, with one propagating faster than the other. This splitting effect results in two variables of extreme relevance for study: delay time (δt) and polarization direction (ϕ).

The delay time is observed through the arrival of pulses at the station, where the difference between the fast and slow pulses results in what is termed δt . The variation in the value of delay time is proportionate to the thickness of the anisotropic layer or the fault with which the wave interacts. The observed pulses originate from the splitting of the XK(K)S phases ($X = P$ or S), which are capable of interacting with the core-mantle boundary, and their refraction is predominantly vertical in relation to the station.

Regarding the polarization direction, this parameter generally indicates the preferential orientation of the lattice of anisotropic minerals present in the mantle, which is a result of mantle shear deformation. The mantle composition is predominantly Olivine (65% vol), thus inferring that the fast polarization directions result from the interaction of the shear wave with Olivine [14].

Olivine is a nesosilicate mineral with a "closed" chemical formula calculation, meaning its chemical composition is consistently close to 100%. It exhibits strong elastic anisotropy [1]. The crystallographic growth axis is [001] (c-axis); however, for seismic anisotropy studies, the [100] axis (a-axis) is considered due to its higher wave propagation velocity for P-waves compared to other axes. Additionally, a study by [14] analyzed over 700 naturally deformed peridotites, revealing that 95% of the samples exhibited a dominant crystal preferred orientation (CPO) along the A-axis.

The CPO of olivine arises from the limited number of dislocation systems the mineral possesses. When subjected to deformation, the crystal aggregate undergoes rotation according to the preferred direction of the deformation, establishing a relationship between asthenospheric flow and mineral preferred orientation [14]. According to [7], for olivine to exhibit a dominant CPO along the [100] axis, the mineral must be in a high-temperature environment with moderate pressure values, low water content, and under the influence of a shear zone.

Olivine presents three possible deformation mechanisms: diffusion creep, dislocation creep, and grain boundary. Due to the study being conducted in a stable continental zone, dislocation creep predominates, primarily along the crystallographic [100] axis, allowing for a straightforward relationship between Olivine CPO and seismic anisotropy, thereby determining mantle flow through anisotropic parameters.

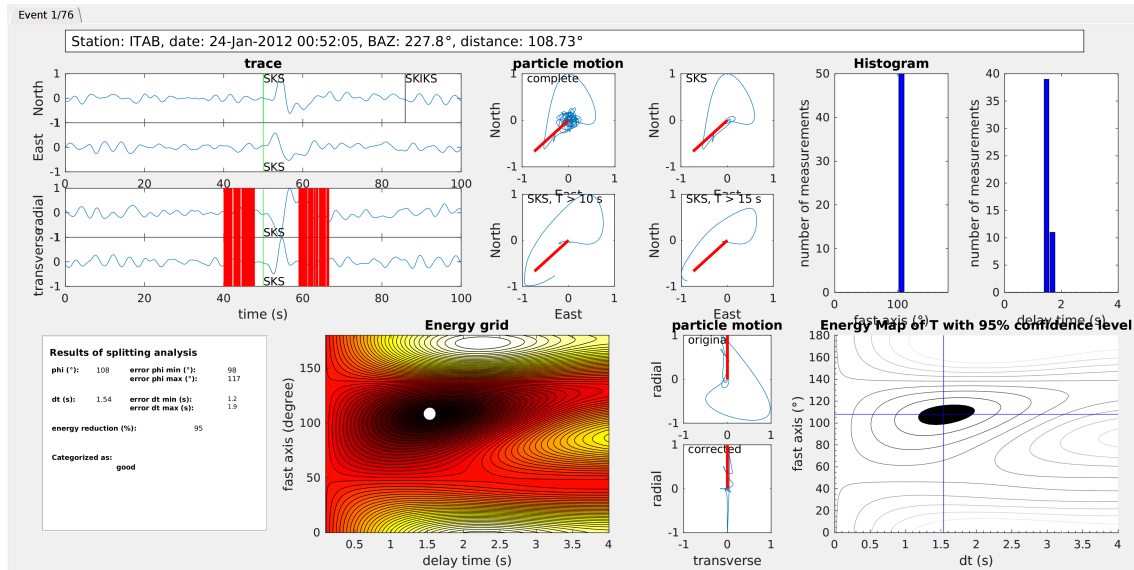


Figure 2. Analysis of one of the XK(K)S phases from station ITAB. In the upper left part with the title "trace," we have the phase without the change in sensor orientation (East and North), and below we have the phase with the change in sensor orientation (transverse and radial); the vertical red bars represent random time windows around the phase. The histograms correspond to the delay time and polarization direction (ϕ) parameters, resulting from the analysis of the 50 time windows selected by the program. The Energy grid and Energy map are used to choose the best region to reduce energy in the transverse component. The particle motion at the bottom shows the particle's movement without correction of the transverse component (original) and the particle's linearized movement after correction (corrected). The results of splitting analysis display the parameters, their respective errors, and the percentage of energy reduction in the transverse component.

Diffusion deformation can be observed in regions with high pressure, hydration, and stress, resulting in a shift in Olivine's preferred axis from [100] to [001]. Consequently, the C-axis aligns with the flow direction and rapid wave propagation. This explains the parameter changes observed in [4] study in the Andes region, as well as elucidating the orientation shift and reduction in anisotropic parameters of the upper mantle at depths below 250 km.

2. Data and Methods

The data used in this study were obtained from the University of São Paulo (USP) network through the FDSN request. The analyzed stations were those available in the Brazilian Seismograph Network (RSBR), covering a large part of the Brazilian territory, especially the northern, central-western, and southeastern regions. A total of 72 stations and over 1700 Shear Wave Splitting data were analyzed, providing new parameters for seismic anisotropy studies and updated maps.

The phases used were generally the XK(K)S phases, which have a relatively wide propagation radius, corresponding to an epicentral window of 85° to 130° . Furthermore, the XK(K)S phase has a longer travel path, reaching great depths, as it travels from the seismic wave source to the outer core and is then reflected back to the receiver, thus carrying information about the physical parameters in the subsurface. Only data with a signal-to-noise ratio equal to or greater than 2.5 were used to ensure the reliability of the obtained parameters for analysis [21].

Among the various techniques developed over the years to analyze seismic phases and obtain estimates of fast polarization direction and delay time, this study utilized methods developed by [23]. These include the Silver and Chan method for error measurement Figure 2, sensor misorientation analysis, and the grid of the mean energy reduction of the transverse component, in addition to employing statistical bootstrap calculations for error estimates Figure 3.

For data analysis, the MATLAB-based software SplitRacer [21], along with the automation package developed by [20], was employed. The method devised by [23] aims to minimize energy in the transverse component; however, the

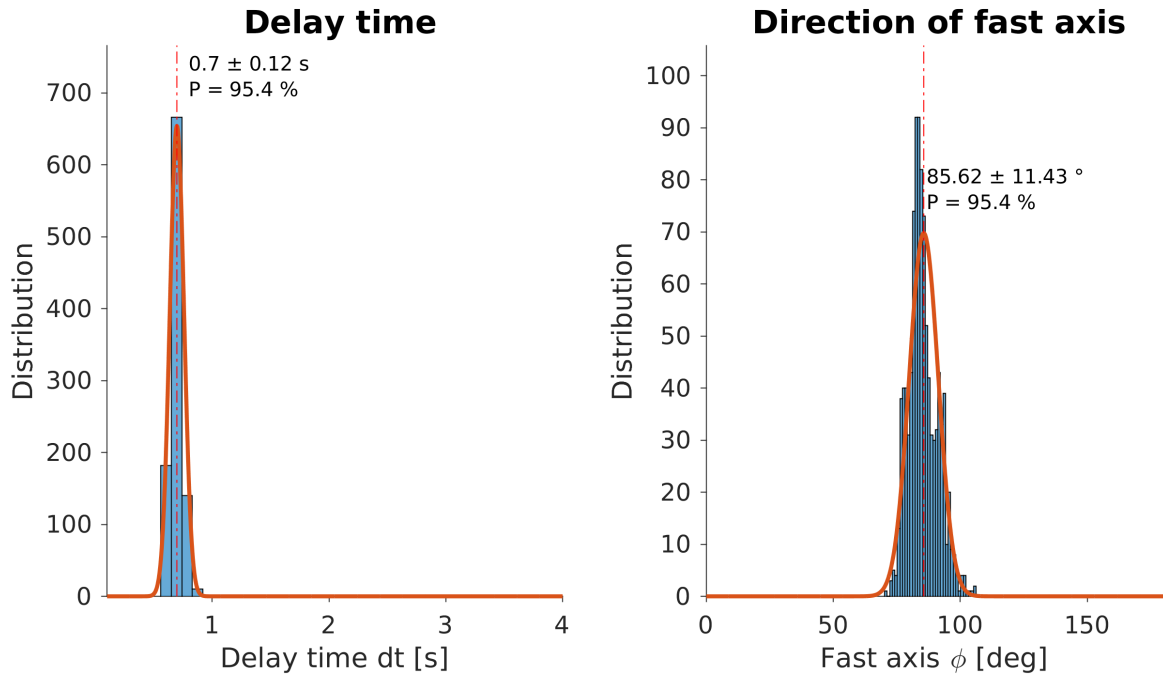


Figure 3. Anisotropic parameters obtained through the bootstrap technique at station IPMB, displaying the distribution of observed values (blue bars), the normal distribution curve (orange line), and the estimated value for the parameters (dashed orange vertical line).

authors' calculations contained a derivation error, as noted by [24].

The energy minimization method in the transverse component entails employing a wave propagation formula in an isotropic environment, where wave interaction with a particle results in linear motion. Subsequently, a division operator is applied, incorporating parameters of fast polarization direction and delay time into the formula. It is then necessary to determine suitable parameter values that will revert the formula to isotropic medium propagation (linear particle motion). SplitRacer calculates a reduced average energy grid across all selected time windows (defaulting to 50 time intervals around the phase), with a reliability percentage of 95 Figure 2. The code lines for this task are based on those used by [26] during the development of their SplitLab software, which also aids in shear wave splitting analyses. Upon obtaining the parameters, the reverse division operator is applied, offering superior efficiency in transverse component energy reduction.

In theory, subsequent to the application of the reverse division operator, particle motion should undergo linearization, and the minimization of transverse component energy should occur. If linearization of particle motion is not achieved following this procedure, the data are deemed poor and discarded for analysis and final results. In some instances, shear wave splitting fails to occur, or pulses propagate parallelly post-division; this phenomenon is classified as null and discussed in the presence of complex anisotropic structures, as addressed by [6] and [19], who observed abnormal values east of SE Brazil.

During the preprocessing steps of the XK(K)S phases within SplitRacer, an analysis of sensor misalignment at a station is performed based on seismic phases visualized and saved in the visual quality check section. [3] showed that some stations of the RSBR have orientation issues, which may be reinforced in this study. If the mean misalignment calculated by the program exhibits a large dispersion across all data, it becomes necessary to assess the possibility of using the misalignment provided by each phase instead of adopting the station's mean misalignment value. For values exceeding 10° , applying a correction becomes necessary [8]. In any case, the information is saved to allow the user to decide later which option to apply in the data processing. The data are evaluated based on particle motion correction and the extent of energy reduction in the vertical component. Energy reduction values below 60% are classified as "poor", values between 70% and 90% as "average", and above 95% as "good" Figure 2. For the final analysis, only data classified as "good" and "average" are considered, while those classified as "poor" are discarded.

Upon completion of the analysis, the statistical technique of bootstrap is employed. Conceived by [15], bootstrap is a statistical method used to investigate the distributional characteristics of a random variable. Typically, this technique is employed when the distribution in question demands a complex analytical evaluation. The term "bootstrap" derives from the expression "to pull oneself up by one's bootstrap", wherein the statistical context, this phrase is used to illustrate that it is possible to infer properties of large samples from a limited number of observations.

Operationally, bootstrap performs sampling with replacement, generating a series of samples of equal size to the original sample. Through "x" draws, where "x" represents the number of observations available in the original sample with replacement, bootstrap samples are produced. This process is repeated "n" times, resulting in "n" bootstrap samples. With these samples, it is possible to construct a distribution curve for the variable of interest. [15] observed that the bootstrap distribution approaches the true distribution as the number of bootstrap samples tends to infinity.

The bootstrap technique is premised on the idea that important parameters can be obtained from a large dataset, making it particularly useful when implemented in the analysis of shear waves. This is due to the large volume of data that various stations present, which allows for the generation of significant bootstrap samples to estimate errors associated with wave division. Based on these considerations, [20] adopted the bootstrap statistical technique to obtain a more precise estimate of errors associated with wave division (Figure 3), presuming a single layer as an assumption.

3. Geological Settings, Results and Discussions

For the initial discussion, we separated the stations by geological provinces using [11] as a reference. These results show that overall the stable South American plate has fast polarization in the East to NNW-SSW direction. The cratons maintain a more NNW-SSW orientation. The Chaco-Paraná basin shows the probably influence of the stable part of the basin (Figure 4). As for the delay time, it shows higher values for fold belts and lower values for cratons (Figure 5).

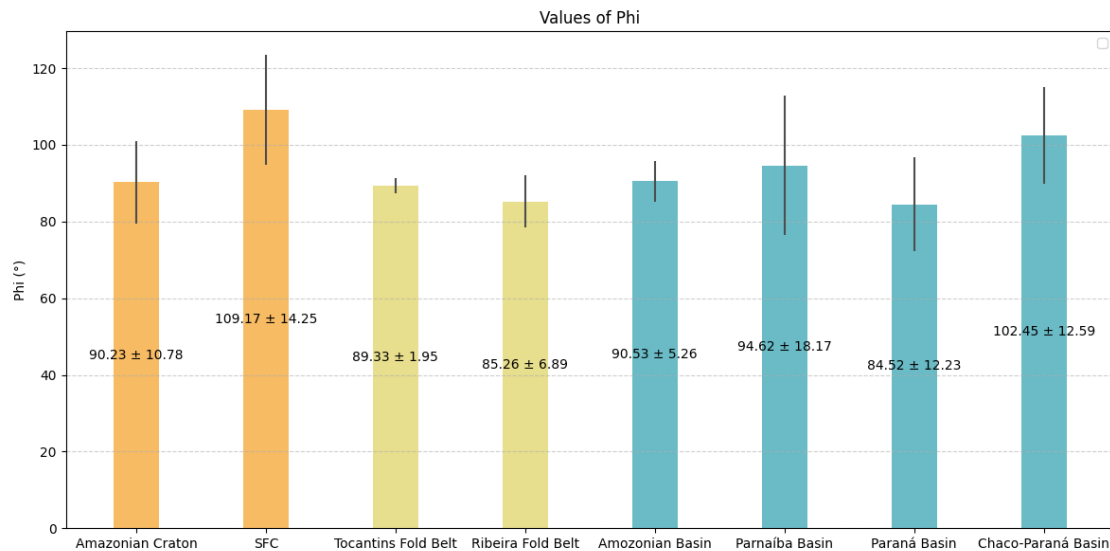


Figure 4. Averages of polarization directions and their respective errors for each province in South America. The yellow bars represent the average values for the cratons, the green bars correspond to the values presented by the fold belts, and the blue bars refer to the basins. The average values of fast polarization direction obtained in the Amazonian craton were derived from 12 stations in the region, while in the São Francisco craton, there were 5 stations. In the Tocantins fold belt, data were obtained from 2 stations, and in the Ribeira fold belt, from 4 stations. For the Amazon basin, the data came from 7 stations, the Parnaíba basin had 3 stations, the Paraná basin had data from 22 stations, and the Chaco-Paraná basin had data from 6 stations. SFC is San Francisco Craton, we used as reference [11]

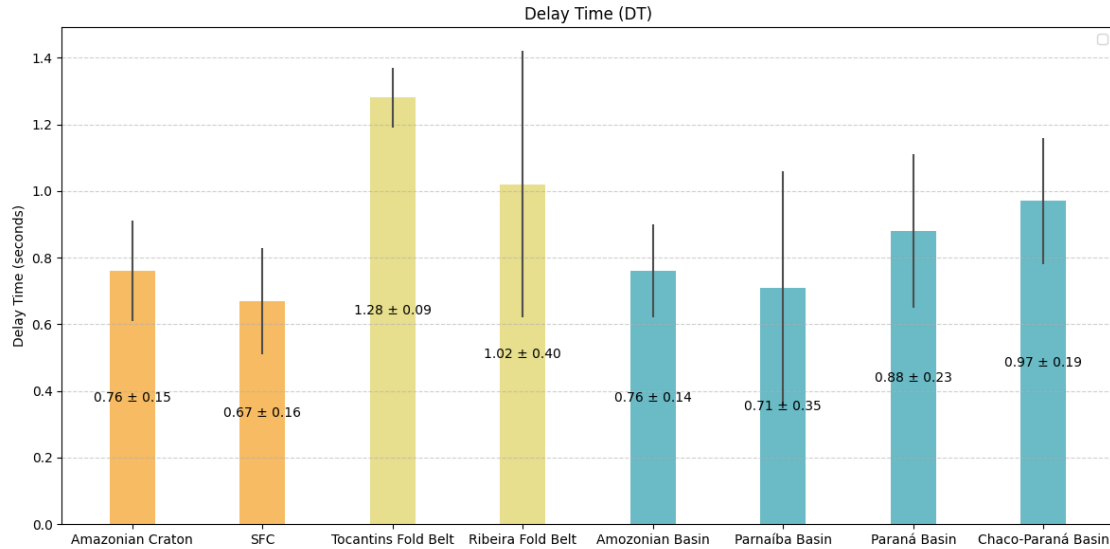


Figure 5. Averages of delay time and their respective errors for each province in South America. The yellow bars represent the average values for the cratons, the green bars correspond to the values presented by the fold belts, and the blue bars refer to the basins. The average values of fast polarization direction obtained in the Amazonian craton were derived from 12 stations in the region, while in the São Francisco craton, there were 5 stations. In the Tocantins fold belt, data were obtained from 2 stations, and in the Ribeira fold belt, from 4 stations. For the Amazon basin, the data came from 7 stations, the Parnaíba basin had 3 stations, the Paraná basin had data from 22 stations, and the Chaco-Paraná basin had data from 6 stations. SFC is San Francisco Craton, we used as reference as [11]

In a study by [4], a correlation between lithospheric boundaries and S-wave anomalies was examined, enabling the visualization of two cratonic roots, namely the Amazonian craton and the São Francisco craton. [26] and [16] observed the behavior of asthenospheric flow in cratonic regions, and their hypotheses have since been widely utilized, including in the context of the Amazonian and São Francisco cratons.

The numerical mantle convection model developed by [10] was employed, in which the author posits that fast polarization direction values correlate with the asthenospheric flow model. This correlation holds true at depths of 225 km, where a strong relationship is observed. However, the correlation weakens in continental regions, suggesting a significant contribution of frozen anisotropy within the continental lithosphere.

The Amazonian craton comprises the Guiana Shield and the southern shields of central Brazil [13] and [2]. The Amazonian craton exhibits a deep root to the south (Figure 6), and through the mantle flow model, a slight deviation around the cratonic root is discerned. The scarcity of stations in the region greatly hampers the ability to infer whether there is a deviation around the cratonic root. However, analysis of station NPGB reveals a slight deviation, potentially indicating a perimeter around the cratonic root to the south of the southern Brazilian shield. Furthermore, there is no correlation between fast polarization directions and mantle flow for stations located in the intracratonic sedimentary basin of the Amazon, although they exhibit fast polarization directions aligned with the absolute plate motion, as noted by [4] for continental regions. The results show low delay times in these regions, likely due to minimal anisotropic influence.

In São Francisco Craton (Figure 6), the fast polarization direction is oriented NW-SE, consistent with the observations by [5]. [5] explained that this orientation is due to the deflection caused by the cratonic root present in the southern São Francisco Craton, which results in a deviation of mantle flow and consequently affects the observed parameters. [5] further demonstrated in their studies that the lithospheric fabric in the southeastern part of the province coincides with the collision between the São Francisco Craton and the Paranapanema Cratonic Block (Figure 6), which could influence fast polarization direction patterns, as posited by [19] and [5]. To the north of the province, fast polarization directions are oriented WSW-ENE, oblique to the Transbrasiliano lineament

In the Fold Belt (Tocantins and Brasília) (Figure 7), [19] suggest that the observed anisotropy values may be related to the Brasiliano accretion cycle, resulting in the Gondwana supercontinent. Thus, this could potentially explain the observed fast polarization directions south of the São Francisco craton as a result of fossilized anisotropy. In the central portion of the craton, S-wave polarizations are oriented NW-SE, corresponding to shear zones present in the region and justifying the high delay time observed by station SDBA. However, more recent studies argue that the observed polarization patterns south of the São Francisco craton and Brasília belt result from the influence of asthenospheric flow, resulting in a preferential direction of olivine according to the flow deviation around the cratonic root.

The Paraná Basin exhibits a slight E-W orientation in its central portion and also presents low delay times, inferior to one second. [5] suggests the possible existence of a cratonic core in the central part of the basin. Although the delay time values are low for a cratonic core, their polarization directions are consistent with the likely presence of such a core. Such observations can be explained by the absolute plate motion or by frozen anisotropy in the lithosphere. However, according to [5], the latter presents difficulty in verification due to sedimentary coverage. Other authors ([5, 12, 8]) conducting studies in the Paraná Basin have observed that to the northeast of the basin, the directions of fast polarization tend to orient NW-SE, following the geological structures of the southern portion of the Brasília Fold Belt.

The polarization directions in the Ribeira Belt (Figure 6) predominantly align towards the WSW-ENE axis. Additionally, they exhibit high delay time values in certain regions, suggesting a thick anisotropic layer. The parameters obtained correspond to those of other researchers, including [5], who suggested that the observed delay time values could be considered among the highest globally. Moreover, the polarization directions seem to align biasedly with the fold structures present in the region, especially in the central portion.

Due to significant tectonic events accumulated over the years, the Northeast region presents a variety of geomorphological structures. Influenced by geological formation factors such as erosion, weathering, magmatism, sedimentation, and climatic variations, the region exhibits complex variables in the global geomorphological scenario ([9]). Despite limited observations in Northeast Brazil, studies conducted by [12] indicated that the polarization directions are oriented N-S, coinciding with local geological structures. Furthermore, a high delay time is observed for stations in the Northeast, indicating the influence of large structures that may be causing these elevated delay time values.

In general, the obtained parameters correspond to those obtained by other researchers. Some stations exhibit a high delay time, such as ITAB located in the Paraná Basin, ESAR and VABB located in the Ribeira Belt (section 4). The parameter database still has much to be explored, especially in the northern part of the Amazon Craton and particularly near regions with a higher Moho depth and regions presenting a high anomaly in S-wave velocity values [12]. The Northeast also requires more information on parameters of upper mantle anisotropy and the possible causes for anisotropic responses, given that there have been few studies focused on this. However, it is important to note that the data in the Northeast do not have such a good signal-to-noise ratio, so working with the region's data should be approached cautiously due to its low signal-to-noise ratio, making the data and results less reliable [6].

4. CONCLUSIONS

The extensive analysis conducted in this paper sheds light on the ongoing exploration of anisotropic phenomena within the Brazilian territory. Despite considerable progress, numerous avenues remain to be explored, and the data collected in this study play a crucial role in bridging existing gaps in Brazil's geological and geophysical knowledge base. Additionally, the reanalysis of stations previously examined by other works has significantly enriched updated datasets, contributing to a understanding of anisotropic phenomena.

The discourse surrounding observed anisotropy in Brazil encompasses a spectrum of theories regarding its genesis. While some works, exemplified by [10], attribute observed polarization directions to the influence of asthenospheric flow on olivine, others propose alternative hypotheses suggesting that polarization directions may stem from regions subjected to significant shearing during historical periods, resulting in "frozen" or "fossilized" anisotropy.

The comprehensive analysis covering over 190 stations across South America intraplate has provided diverse insights into the factors influencing polarization directions. Notably, in the Southern region of the São Francisco Craton and the Southeast of the Tocantins Fold Belt, observed values tend to align with a NW-SE orientation, consistent with previous findings. However, contrasting interpretations by [5] propose different alignments parallel to the Brasília

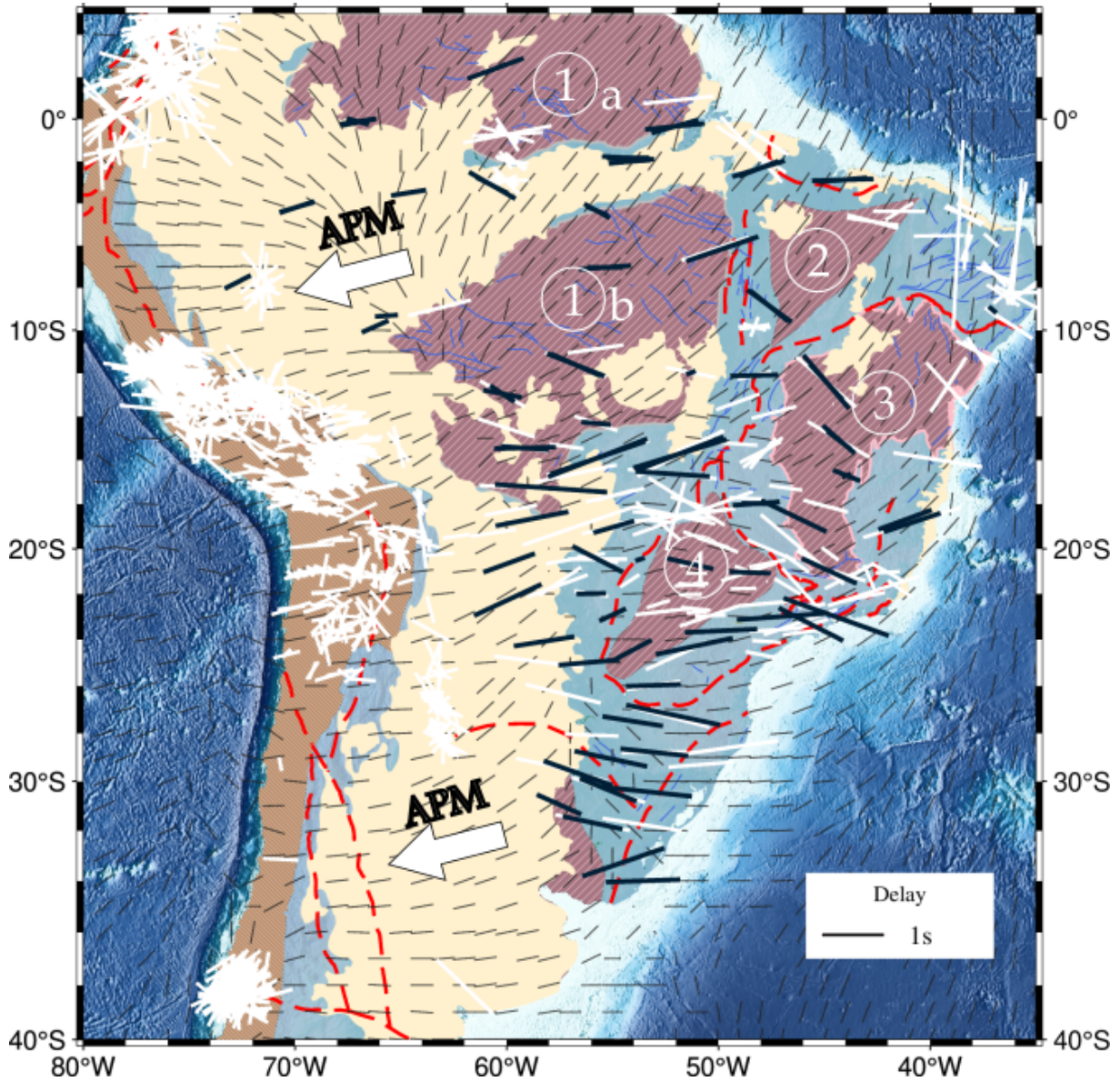


Figure 6. Map showing the main geochronological structures. Plot showing the ϕ and δt parameters, where orientation indicates the directions of fast polarizations and the size of the traces corresponds to the delay time. In the background, the gray lines represent the asthenospheric flow, as elaborated by Conrad et al. [10]. The black lines denote the parameters obtained in this study. The white lines represent parameters obtained by other researchers. The dotted lines represent the suture zones. The yellow region on the map corresponds to the Cenozoic coverage. The blue coverage corresponds to the neoproterozoic belt. The light brown region shows the Andes belt. Map legends are as follows: 1a - Amazon Craton (Guyana Shield); 1b - Amazon Craton (Central Brazil Shield) ; 2 - Parnaíba Craton; 3 - São Francisco Craton; 4 - Paranápanema Block; APM, Absolute Plate Motion direction in the HS3-NUVEL-1A frame [17].

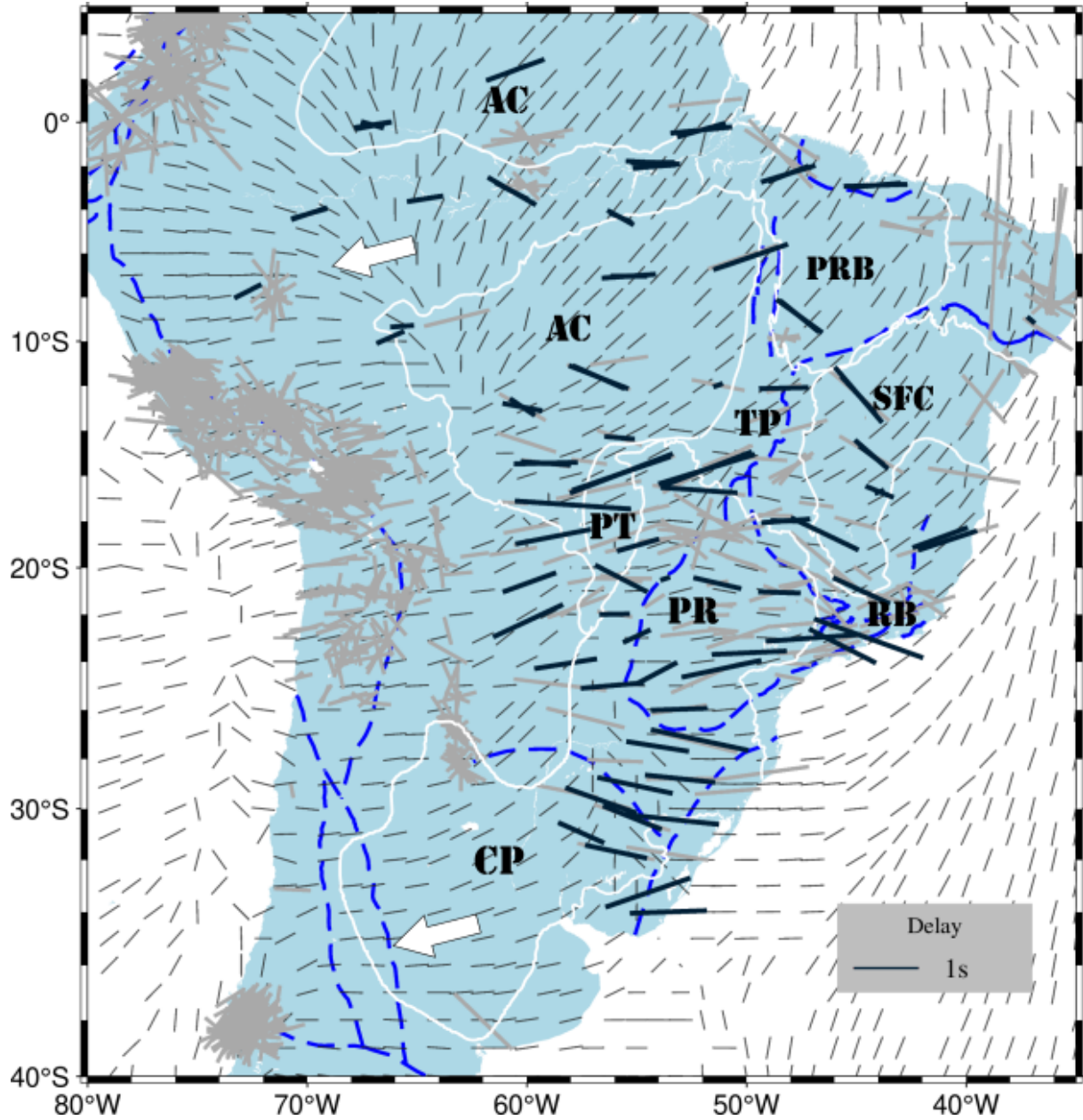


Figure 7. Map showing the main tectonics elements of South America. Plot showing the ϕ and δt parameters, where orientation indicates the directions of fast polarizations and the size of the traces corresponds to the delay time. In the background, the gray lines represent the asthenospheric flow, as elaborated by Conrad et al. [10]. The black lines denote the parameters obtained in this study. The Darkgray lines represent parameters obtained by other researchers. The blue dotted lines represent the suture zones. Map legends are as follows: SFC, São Francisco Craton; AC, Amazon Craton; PR, Paraná Basin; Pt, Pantanal Basin; RB, Ribeira Fold Belt; CP, Chaco Paraná Basin; TP, Tocantins Fold Belt Province; PRB, Parnaíba basin; The white arrows shows Absolute Plate Motion (APM) direction in the HS3-NUVEL-1A frame [17].

folding. In the Northern segment of the Tocantins Fold Belt, polarization directions trend towards a WSW-ENE orientation.

The Amazonian Craton, the main focus of this study, has fewer stations compared to Southeastern Brazil and therefore has limited information about anisotropy in the region. However, even with limited information, some conclusions can be drawn. Overall, the data show a predominant orientation of the polarization directions, mainly in the Amazon Basin, tending towards WSW-ENE. Additionally, it is noteworthy that the WSW-ENE orientation aligns with the absolute plate motion (HS3-NUVEL1A), suggesting a correlation between regional tectonic dynamics and anisotropic behavior. In the center of the Central Brazilian Shield, a study conducted by [2] identified the Moho thickness, indicating a possible cratonic root. It is observed that both the polarization directions and [10] numerical model of mantle flow deviate in the region with greater Moho depth (approximately 60 km). In the northeastern portion of the Central Brazilian Shield, [12] detected S-wave velocity anomalies at a depth of 150 km, indicating a cratonic root. The observed parameters near the region seem to undergo a deflection, suggesting that the polarization directions are under the influence of asthenospheric flow.

While the northeastern region yielded less conclusive results due to signal-to-noise ratio limitations and data categorization issues, observations underscore a propensity for polarization directions to align with geological structures. Parameters obtained closely align with the numerical model proposed by [10]. Given the northeast's complex lithospheric history, observed parameters may predominantly reflect frozen anisotropy. Additionally, the presence of the Potiguar rift may contribute to shear zone formation, potentially leading to elevated delay time values.

Overall, the delay time in stable regions is greater than in mountainous regions, likely indicating preserved anisotropy, except in the Amazon region, which shows a delay time similar to the Andean regions.

In conclusion, the findings presented underscore the intricate interplay between geological processes and anisotropic phenomena within the Brazilian territory. Through multifaceted analysis, this study significantly advances our understanding of anisotropy in South America Intraplate. Continued research efforts aimed at refining methodologies and elucidating underlying mechanisms will be instrumental in further unraveling the complexities of anisotropic behavior within Brazil's geological framework.

ACKNOWLEDGMENTS

This study was financed in part by the Coordenação de Aperfeiçoamento de Pessoal de Nível Superior - Brazil (CAPES) - CNPq (Conselho Nacional de Desenvolvimento Científico e Tecnológico) granted a Research Fellowship (PQ-1C 310240/2020-4) to GSF. Finance Code 001. Figures were prepared using the Generic Mapping Tools (GMT) software package [25].

DATA AVAILABILITY

The data used in this study are available at <http://www.splitwave.vercel.app>, with DOI: <https://doi.org/10.5281/zenodo.10988278>.

References

- [1] Abramson, E. H., J. M. Brown, L. J. Slutsky, and J. Zaugg, 1997, The elastic constants of san carlos olivine to 17 gpa: *Journal of Geophysical Research: Solid Earth*, **102**, no. B6, 12253–12263, doi: 10.1029/97JB00682.
- [2] Albuquerque, D., G. França, L. Moreira, M. Assumpção, M. Bianchi, L. Barros, C. Quispe, and M. Oliveira, 2017, Crustal structure of the amazonian craton and adjacent provinces in brazil: *Journal of South American Earth Sciences*, **79**, doi: 10.1016/j.jsames.2017.08.019.
- [3] Albuquerque, D. F., M. P. Rocha, M. Ianniruberto, G. S. França, R. A. Fuck, M. F. de Paulo, and M. B. Aguiar, 2024, Estimating seismometer component orientation of the brazilian seismographic network using teleseismic p-wave particle motion analysis and directional statistics: *Journal of South American Earth Sciences*, **134**, 104754, doi: 10.1016/j.jsames.2023.104754.
- [4] Assumpcao, M., M. Guarido, S. van der Lee, and J. C. Dourado, 2011, Upper-mantle seismic anisotropy from sks splitting in the south american stable platform: A test of asthenospheric flow models beneath the lithosphere: *Lithosphere*, **3**, no. 2, 173–180, doi: 10.1130/L99.1.
- [5] Assumpção, M., M. Heintz, A. Vauchez, and M. Silva, 2006, Upper mantle anisotropy in se and central brazil from sks splitting: Evidence of asthenospheric flow around a cratonic keel: *Earth and Planetary Science Letters*, **250**, no. 1-2, 224–240, doi: 10.1016/j.epsl.2006.07.038.
- [6] Bastow, I. D., J. Julià, A. do Nascimento, R. Fuck, T. Buckthorp, and J. McClellan, 2015, Upper mantle anisotropy of the borborema province, ne brazil: Implications for intra-plate deformation and sub-cratonic asthenospheric flow: *Tectonophysics*, **657**, 81–93, doi: 10.1016/j.tecto.2015.06.024.

- [7] Bystricky, M., K. Kunze, L. Burlini, and J. P. Burg, 2000, High shear strain of olivine aggregates: Rheological and seismic consequences: *Science*, **290**, no. 5496, 1564–1567, doi: 10.1126/science.290.5496.1564.
- [8] Chagas de Melo, B., and M. Assumpção, 2018, Mantle anisotropy and asthenospheric flow around cratons in southeastern south america: *Geophysical Journal International*, **215**, no. 1, 494–506, doi: 10.1093/gji/ggy288.
- [9] Claudino-Sales, V., C. A. C. B., M. K.A., and M. R. P., 2022, *in* (2022). 30. Estado da Arte dos Estudos Geomorfológicos no Nordeste Brasileiro: Uma síntese e (E várias Teses).: 849.
- [10] Conrad, C. P., M. D. Behn, and P. G. Silver, 2007, Global mantle flow and the development of seismic anisotropy: Differences between the oceanic and continental upper mantle: *Journal of Geophysical Research: Solid Earth*, **112**, no. B7, doi: 10.1029/2006JB004608.
- [11] Cordani, U. G., V. A. Ramos, L. M. Fraga, M. Cegarra, I. Delgado, K. G. d. Souza, F. E. M. Gomes, and C. Schobbenhaus, 2016, Tectonic map of south america: scale 1:5 000 000: explanatory notes: Commission for the Geological Map of the World.
- [12] de Andrade, M. G., 2008, Anisotropia sísmica do manto superior na américa do sul com a divisão de ondas sks.
- [13] de Sousa Nascimento, A. V., G. S. França, C. Alberto, M. Chaves, and G. S. Marotta, 2021, Rayleigh wave group velocity maps at periods of 10–150s beneath south america: *Geophysical Journal International*, doi: 10.1093/gji/ggab363.
- [14] Demouchy, S., Q. Wang, and A. Tommasi, 2023, Deforming the upper mantle—olivine mechanical properties and anisotropy: *Elements*, **19**, no. 3, 151–157, doi: 10.2138/gselements.19.3.151.
- [15] Efron, B., 1979, The 1977 rietz lecture. bootstrap methods: Another look at the jackknife: *The Annals of Statistics.*, **7**, 1–26.
- [16] Fouch, M. J., K. M. Fischer, E. M. Parmentier, M. E. Wysession, and T. J. Clarke, 2000, Shear wave splitting, continental keels, and patterns of mantle flow: *Journal of Geophysical Research: Solid Earth*, **105**, no. B3, 6255–6275, doi: 10.1029/1999JB900372.
- [17] Gripp, A. E., and R. G. Gordon, 2002, Young tracks of hotspots and current plate velocities: *Geophysical Journal International*, **150**, no. 2, 321–361, doi: 10.1046/j.1365-246X.2002.01627.x.
- [18] Hess, H. H., 1964, Seismic anisotropy of the uppermost mantle under oceans: *Nature*, **203**, no. 4945, 629–631, doi: 10.1038/203629a0.
- [19] James, D. E., and M. Assumpção, 1996, Tectonic implications of $i\epsilon_s/i\epsilon_c$ -wave anisotropy beneath se brazil: *Geophysical Journal International*, **126**, no. 1, 1–10, doi: 10.1111/j.1365-246X.1996.tb05263.x.
- [20] Link, F., M. C. Reiss, and G. Rumpker, 2022, An automatized xks-splitting procedure for large data sets: Extension package for splitracer and application to the usarray: *Computers Geosciences*, **158**, 104961, doi: 10.1016/j.cageo.2021.104961.
- [21] Reiss, M. C., and G. Rumpker, 2017, Splitracer: Matlab code and gui for semiautomated analysis and interpretation of teleseismic shear-wave splitting: *Seismological Research Letters*, **88**, no. 2A, 392–409, doi: 10.1785/0220160191.
- [22] Silver, P. G., 1996, Seismic anisotropy beneath the continents: Probing the depths of geology: *Annual Review of Earth and Planetary Sciences*, **24**, no. 1, 385–432, doi: 10.1146/annurev.earth.24.1.385.
- [23] Silver, P. G., and W. W. Chan, 1991, Shear wave splitting and subcontinental mantle deformation: *Journal of Geophysical Research: Solid Earth*, **96**, no. B10, 16429–16454, doi: 10.1029/91JB00899.
- [24] Walsh, E., R. Arnold, and M. K. Savage, 2013, Silver and chan revisited: *Journal of Geophysical Research: Solid Earth*, **118**, no. 10, 5500–5515, doi: 10.1002/jgrb.50386.
- [25] Wessel, P., J. F. Luis, L. Uieda, R. Scharroo, F. Wobbe, W. H. Smith, and D. Tian, 2019, The generic mapping tools version 6: *Geochemistry, Geophysics, Geosystems*, **20**, no. 11, doi: 10.1029/2019GC008515.
- [26] Wüstefeld, A., G. Bokelmann, C. Zaroli, and G. Barruol, 2008, Splitlab: A shear-wave splitting environment in matlab: *Computers Geosciences*, **34**, no. 5, 515–528, doi: 10.1016/j.cageo.2007.08.002.

Appendix A. Table of results

Table A.1: Shear wave splitting stations and parameters, with respective errors

Station	Lat	Lon	ϕ	δt	std ϕ	std δt
AGBL	-9.04	-37.05	131	0.10	73	0.21
ALGR	-28.80	-53.03	96	1.03	3.5	0.05
AMBA	-22.93	-54.99	65	0.41	2.5	0.05
ANTJ	-22.00	-56.00	89	0.41	8	0.10
AQDB	-20.48	-55.70	117.27	0.855	10.56	0.24
ARAG	-15.71	-51.81	69	1.44	1.5	0.10
ARAP	-30.95	-57.52	114	0.72	18	0.31
BBLB	-18.67	-58.80	79	1.13	2.5	0.15
BEB11	-21.07	-48.50	92.00	0.6	0.8	0.08
BOAV	2.40	-60.52	69.88	0.58	2.26	0.3
BSCB	-21.00	-44.76	114.58	0.91	7.37	0.23
BSFB	-18.83	-40.85	71.67	0.9	9.75	0.54
CCRS	-17.29	-57.90	94	1.74	3.5	0.21
CPSB	-30.41	-53.44	96.04	1.44	1.27	0.1
CRSM	-27.49	-54.04	99	0.92	5	0.05
CZSB	-7.73	-72.70	75	0.00	12.5	0.05
DVLD	-16.64	-52.16	94	1.13	3.5	0.10
ESAR	-23.02	-44.44	109.70	1.73	3.1	0.27
ETMB	-9.82	-66.21	102.03	1.48	2.06	0.08
FDPY	-22.28	-59.94	65	1.13	3.5	0.36
FRBT	-25.98	-53.06	88	0.82	3.5	0.05
IPMB	-17.98	-48.21	109.65	1.11	2.4	0.08
ITAB	-27.23	-52.13	117.00	1.1	0.8	0.08
ITQB	-29.66	-56.63	109.65	1.11	2.4	0.08
ITTB	-4.37	-55.73	113	0.31	6	0.00
JANB	-15.06	-44.31	131	0.62	3	0.10
LABB	-9.32	-65.68	115.61	1.1	4.47	0.13
MACA	-3.00	-60.68	78.00	1.2	0.8	0.08
MAL2	-2.02	-54.18	87.30	1.1	7.45	0.36
MALB	-1.85	-54.26	69.87	0.85	9.06	0.22
MAPY	-20.64	-59.88	70	0.82	2	0.10
MC01	-16.71	-43.94	69	0.10	45	0.26
MCPB	-0.3602	-52.06	103.00	0.7	0.8	0.08
MCR1	-24.46	-54.04	62	0.62	3	0.15
NBRS	-14.32	-55.78	95	0.41	8.5	0.05
NPGB	-7.05	-55.36	85.85	1.41	4.9	0.08
PAPY	-24.09	-58.23	81	0.92	9	0.36
PARB	-23.34	-45.62	-	-	-	-
PDRB	-11.61	-56.73	85.62	0.7	11.43	0.12
PEXB	-12.11	-48.30	-	-	-	-
PMNB	-18.54	-46.44	119.89	0.8	11.01	0.09
PRPB	-6.17	-49.82	-	-	-	-
PTLB	-15.45	-59.14	93.13	0.78	9.48	0.11
RODS	-30.35	-55.20	112	0.92	4.5	0.15

Continues on the next page

Station	Lat	Lon	ϕ	δt	sdt ϕ	std δt
ROIB	-24.30	-51.14	84.24	0.9	48.35	0.55
ROSB	-2.90	-44.12	85.87	0.78	9.52	0.14
ROST	-34.00	-53.55	88	1.13	6.5	0.15
RPRD	-20.48	-53.70	72	0.10	19.5	0.10
RVDE	-19.03	-54.94	74	0.62	4	0.05
SALB	-15.90	-55.69	69	1.64	3	0.31
SALV	-15.90	-55.69	71	1.54	0.5	0.05
SDBA	-12.41	-44.90	111.38	0.93	4.86	0.14
SGC2	-0.15	-66.98	71.09	1.16	3.81	0.28
SGCB	-0.12	-67.03	81	0.51	6	0.10
SICB	-23.63	-49.88	88.51	0.93	4.59	0.1
SJMB	-18.71	-41.18	88.22	0.93	6.79	0.12
SJPY	-25.00	-56.10	85	0.92	3	0.05
SMTB	-8.86	-47.59	129	0.72	2	0.05
SNDB	-11.97	-51.29	70	0.10	28.5	0.21
TBOT	-31.68	-55.94	102	0.92	4	0.10
TBTG	-4.19	-69.91	139.57	1.07	2.18	0.15
TEFE	-3.51	-64.63	81	0.41	4	0.05
TMAB	-2.37	-48.10	69	0.62	43	0.87
TRIB	-20.67	-51.33	-	-	-	-
UNIS	-29.07	-55.07	102	1.13	4.5	0.10
VABB	-23.00	-46.97	71.44	0.53	7.93	0.67
VILB	-12.95	-60.20	100.54	0.57	49.19	0.3
VSTT	-33.26	-54.49	71	1.33	5	0.31

4 RESULTS AND DISCUSSION

The discussion about the observed anisotropy in Brazil involves different hypotheses about this. [Conrad, Behn and Silver \(2007\)](#) argue that the observed polarization directions result from the influence of asthenospheric flow on olivine, especially at depths of up to 225 km, which correlates better with data observed in oceanic regions ([Assumpção et al., 2011](#)). On the other hand, there are researchers who attribute the polarization directions to regions that underwent strong shearing at some historical moment, resulting in what is called frozen or fossilized anisotropy, which records seismic activities from a certain geological period.

In Brazil, with more than 70 analyzed stations, there is a variety of information about the influences on polarization directions. In the southern region of the São Francisco Craton and in the southeast of the Tocantins Fold Belt, the observed values tend to follow an orientation that contours the cratonic root (NW-SE), in line with [Conrad, Behn and Silver \(2007\)](#). However, [Assumpção et al. \(2006\)](#) suggest that the values in the region are parallel to the Goiânia fold, resulting from the collision of the Paranapanema cratonic block under the Paraná Basin and the São Francisco Craton. In the northern portion of the Tocantins Fold Belt, the values are oriented WSW-ENE. It is noteworthy that the delimitation of the São Francisco Craton's depth differs from surface delineations, potentially situating the cratonic root just below the Brasília Belt. This could explain the observed "opening" of fast polarization directions.

However, [Melo et al. \(2018\)](#), in his work, reports that the parameters observed in southeastern Brazil have little influence from geological structures, tending to be practically zero, which contradicts what was supported by other authors ([James and Assumpção \(1996\)](#); [Assumpção et al. \(2006\)](#); [Andrade and Assumpção \(2008\)](#)).

In his work, [Melo et al. \(2018\)](#) correlates the fast polarization directions with the velocities of S-waves at depth. It is observed that at 300 km depth, the polarization directions tend to follow the asthenospheric flow, ruling out the hypothesis of geological structure influence in SE Brazil. In the Paraná Basin, the observed delay time values are low, and the polarization directions align with the absolute plate motion, as presented by [Assumpção et al. \(2011\)](#). In contrast, in the Pantanal Basin, the delay time values are high, and their polarization directions also tend to align with the absolute plate motion. In the Chaco-Paraná Basin, the values tend to rotate to the NW-SE direction; the same was observed by [Melo et al. \(2018\)](#), who correlated the fast polarization directions with the asthenospheric flow model obtained through anisotropic surface waves.

The Amazonian Craton has fewer stations than Southeastern Brazil, hence information on anisotropy in the region is sparse. However, it is feasible to draw certain conclusions. Overall, the data show a predominant orientation of the polarization directions, mainly in the Amazon Basin, tending towards WSW-ENE. Additionally, it is noteworthy that the WSW-ENE orientation aligns with the absolute plate motion (HS3-NUVEL1A), suggesting a correlation between regional tectonic dynamics and anisotropic behavior.

In the center of the Central Brazilian Shield, a study conducted by [Rosa-Costa et al. \(2006\)](#) identified the Moho thickness, indicating a possible cratonic root. It is observed that both the polarization directions and [Conrad, Behn and Silver \(2007\)](#) numerical model of mantle flow deviate in the region with greater Moho depth (approximately 60 km). In the northeastern portion of the Central Brazilian Shield, [Feng, Lee and Assumpção \(2007\)](#), [Nascimento et al. \(2024\)](#) detected S-wave velocity anomalies at

a depth of 150 km, indicating a cratonic root. The observed parameters near the region seem to undergo a deflection, suggesting that the polarization directions are under the influence of asthenospheric flow.

The data for Borborema province show multiple "poor" classifications that have been discarded. Preliminary observations indicate that the polarization directions align with geological formations, as observed by [James and Assumpção \(1996\)](#). However, the parameters determined by the authors are also consistent with the [Conrad, Behn and Silver \(2007\)](#) numerical model.

4.1 Analysis of Direction of Polarization (ϕ) and Delay time (Δt) Values

In this work, the analysis of Phi values demonstrates notable differences and similarities when juxtaposed with the findings from [Melo et al. \(2018\)](#) (Figure 2). The average of fast direction polarization value observed in this study is 92.38° , marginally lower than the 95.76° reported by [Melo et al. \(2018\)](#). This study exhibits a higher standard deviation of 20.80° , as opposed to 17.96° in the earlier study, indicating increased variability in the ϕ values. Such variability may be reflective of regional geological differences or variations in the methodologies employed for data collection. The mean difference in ϕ values between the studies is -0.71 , suggesting that, on average, this study records slightly lower ϕ values.

Similarly, the analysis of Delay time (Δt) values in this study averages at 0.87, which is lower than the 1.06 reported by [Melo et al. \(2018\)](#). The standard deviation for Δt values here is 0.47, compared to 0.34 in the previous study, suggesting a broader range of variation in the delay times recorded. The mean difference in Δt values is -0.20 , indicating that this study generally observes shorter delay times.

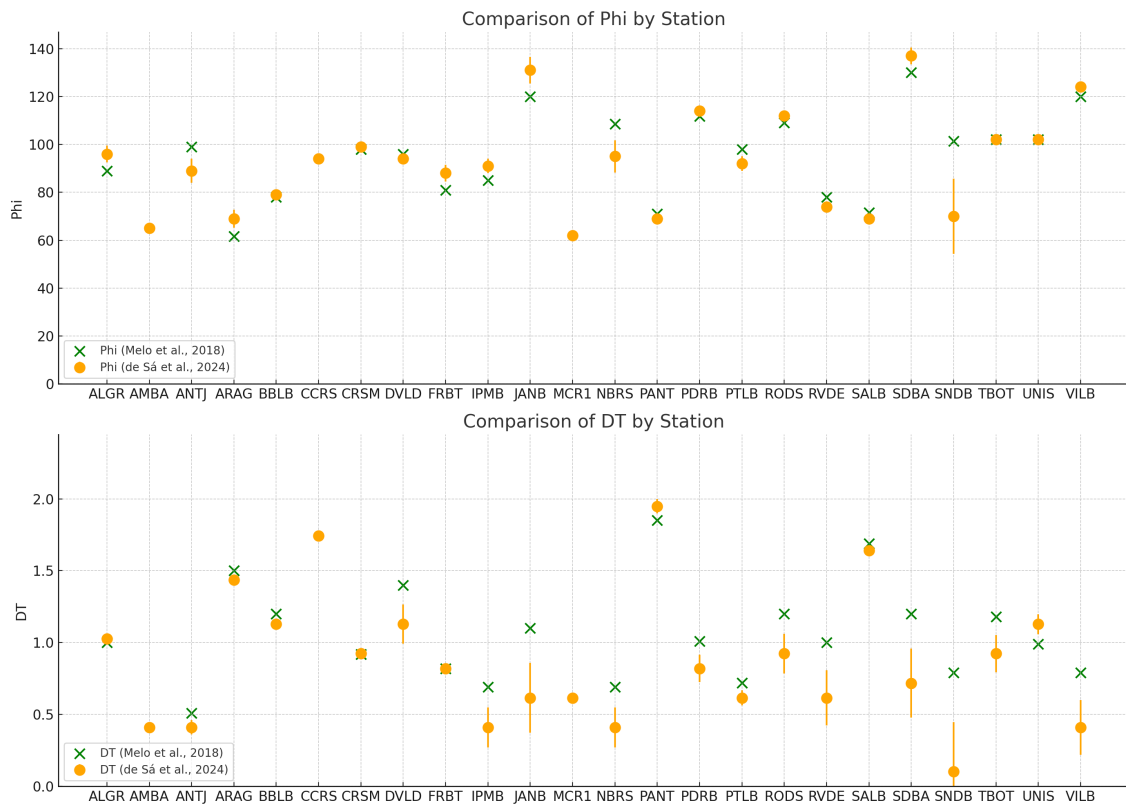


Figure 2 – Comparative graphs of ϕ (Phi) and Δt (Dt) values for each station, between data from [Melo et al. \(2018\)](#) and those obtained for this study. Error bars were calculated as the difference between data from [Melo et al. \(2018\)](#) and those of these studies.

The average polarization direction and delay times in the Amazonian Craton region were found to be $90.23^\circ \pm 10.78^\circ$ (Figure 3) and 0.76 ± 0.15 seconds (Figure 4), respectively, in agreement with

values reported in previous studies (Melo et al. (2018), Assumpção et al. (2006), Assumpção et al. (2011), Andrade and Assumpção (2008), James and Assumpção (1996)). In general, the directions are consistent with the absolute plate motion (ENE-WSW), with only a few stations deviating from this direction. According to Melo et al. (2018), the deviating parameters coincide with the geological features found in the Craton, which may explain the occurrence of diverging polarization directions. Another well-known Craton is the São Francisco Craton, which shows average values of $109.17 \pm 14.25^\circ$ and 0.67 ± 0.16 seconds. The values in the southern part of the Craton seem to be oriented according to geological structures from the Brasiliano orogeny period, resulting in a fold belt. Thus, the observed anisotropy would be the result of "frozen" anisotropy. Conversely, the parameters appear to deflect south of the São Francisco Craton, which may also be explained by the influence of asthenospheric flow. Melo et al. (2018) suggests that it makes more sense for the observed parameters to be influenced by asthenospheric flow rather than geological structures.

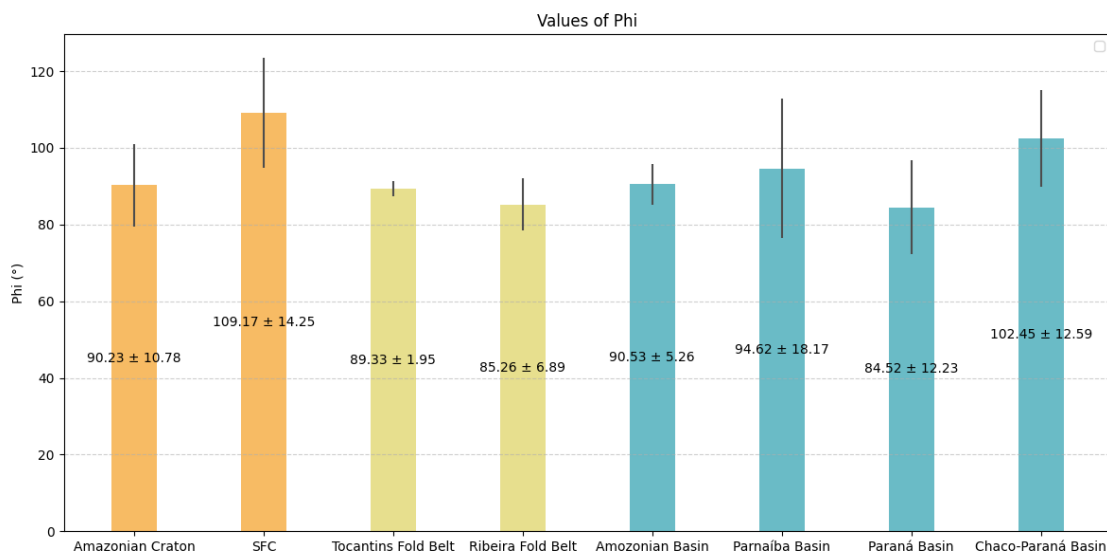


Figure 3 – Averages of polarization directions and their respective errors for each province in South America. a) The orange bars represent the average values for the cratons, the pale yellow bars correspond to the values presented by the fold belts, and the blue bars refer to the basins. b) The average values of fast polarization direction obtained in the Amazonian craton were derived from 12 stations in the region, while in the São Francisco craton, there were 5 stations. c) In the Tocantins fold belt, data were obtained from 2 stations, and in the Ribeira fold belt, from 4 stations. d) For the Amazon basin, the data came from 7 stations, the Parnaíba basin had 3 stations, the Paraná basin had data from 22 stations, and the Chaco-Paraná basin had data from 6 stations. SFC is San Francisco Craton, we used as reference (Cordani et al., 2016)

In the Tocantins Province, the parameters show values of $89.33^\circ \pm 1.95^\circ$ and 1.28 ± 0.09 seconds, and seem to be undergoing "opening." According to Andrade and Assumpção (2008), the delimitation of the São Francisco Craton's root is different from the surface delimitation, with the root lying beneath the Brasília Belt. This would result in a deflection of parameters around the region. In the Paraná Basin, the average values obtained were $84.52^\circ \pm 12.23^\circ$ and 0.88 ± 0.23 seconds. The delay time in the region is generally low and consistent with results obtained by Melo et al. (2018). An important detail is the presence of the Paranapanema Cratonic Block, with values similar to those obtained in other cratons, such as the Amazonian and São Francisco Cratons. Overall, the values are oriented according to the absolute plate motion (ENE-WSW). However, in the northeastern part of the basin, the values are almost horizontal (E-W), tending towards WNW-ESE, likely due to the influence of the deflection occurring south of the São Francisco Craton, indicating asthenospheric flow influence.

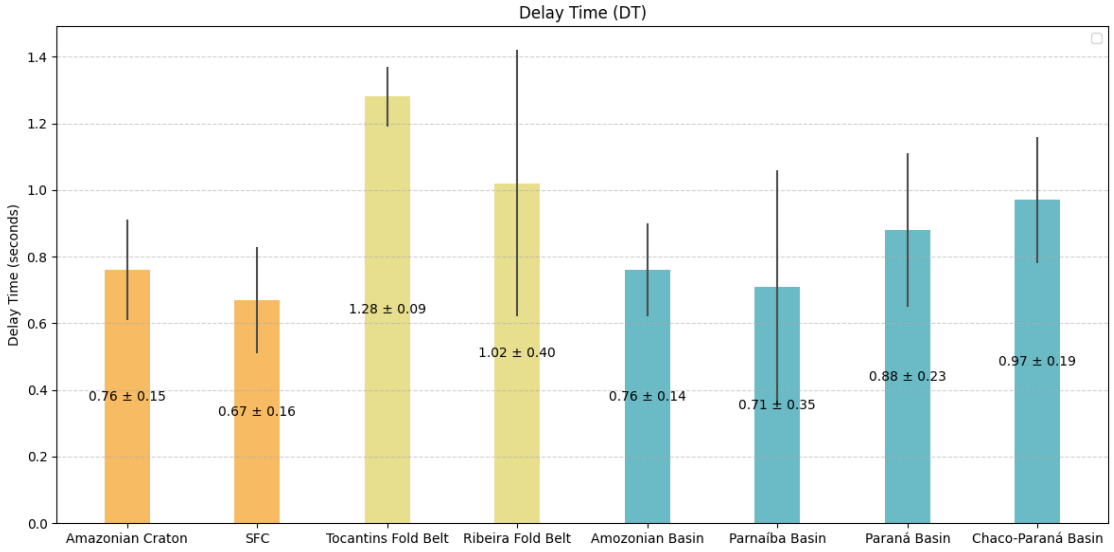


Figure 4 – Averages of delay time and their respective errors for each province in South America. a) The orange bars represent the average values for the cratons, the pale yellow bars correspond to the values presented by the fold belts, and the blue bars refer to the basins. b) The average values of fast polarization direction obtained in the Amazonian craton were derived from 12 stations in the region, while in the São Francisco craton, there were 5 stations. c) In the Tocantins fold belt, data were obtained from 2 stations, and in the Ribeira fold belt, from 4 stations. d) For the Amazon basin, the data came from 7 stations, the Parnaíba basin had 3 stations, the Paraná basin had data from 22 stations, and the Chaco-Paraná basin had data from 6 stations. SFC is San Francisco Craton, we used as reference as (Cordani et al., 2016)

Data obtained near the Chaco-Paraná Basin show values of $102.45^\circ \pm 12.59^\circ$ for polarization direction and 0.97 ± 0.19 seconds for delay time. The polarization directions seem to be rotating, possibly due to the influence of asthenospheric flow and the presence of the Paranapanema Cratonic Block. The Ribeira Fold Belt has values of $85.26^\circ \pm 6.89^\circ$ and 1.02 ± 0.4 seconds, with an average delay time above 1 second, indicating the presence of a thick anisotropic layer. James and Assumpção (1996) suggests that these values result from the collision of the São Francisco Craton with the Paraná Basin and the Paranapanema Cratonic Block. Conversely, Melo et al. (2018) states that in southeastern Brazil, the influence is due to asthenospheric flow.

The Parnaíba Basin includes a cratonic block, with average values of $94.62^\circ \pm 18.17^\circ$ for polarization direction and 0.71 ± 0.35 seconds for delay time. The number of stations analyzed was not as numerous as in other regions, but the values are consistent with Andrade and Assumpção (2008), who reported that the values in the region align with the geological structures present.

Tec. Elements	std ϕ	std δt
Cratons	99.70	0.715
Fold Belts	87.30	1.15
Basins	93.03	0.83

Table 1 – Average of ϕ and Δt for the main elements tectonics of South America

Overall, the parameters observed in the cratonic regions have an average polarization direction of 99.70° and a delay time of 0.72 seconds (Table 1). The basins exhibit average values of 93.03° and 0.83 seconds (Table 1). The fold belts have average values of 87.30° and 1.15 seconds (Table 1). The high delay time is characteristic, but it is important to note that the polarization directions vary due to the distinct nature of these regions, and the ϕ parameters will have different orientations.

5 TECHNOLOGIES USED IN THE DEVELOPMENT OF THE SPLITWAVE FRAMEWORK

In this chapter, we will delve into the technologies employed in the development of the Splitwave framework (Figure 6), conceived with the specific purpose of optimizing the collection, processing, and visualization of geophysical data related to upper mantle anisotropy in Brazil. The fundamental objective of this work is to establish the first Brazilian database dedicated to upper mantle anisotropy, providing a comprehensive platform for storing, analyzing, and sharing geophysical data relevant to the scientific community.



Figure 5 – SplitWave Application Homepage: The application already includes the data presented in this study.

5.1 Back-end: Technologies and Operation

5.1.1 Node.js

Node.js is a JavaScript runtime environment based on the Google Chrome V8 engine, designed to build scalable network applications. In the context of the Splitwave framework, Node.js is used to develop the API server, responsible for managing requests and responses between the front-end and the database.

5.1.2 Hono

Hono is a Node.js framework focused on building efficient and scalable servers. It provides a modular architecture that facilitates the development of RESTful APIs and the integration of different system components. In Splitwave, Hono is employed to ensure smooth communication between the front-end and the back-end, allowing agile and reliable interaction.

5.1.3 Prisma

Prisma is a Node.js Object-Relational Mapping (ORM) designed to simplify access and manipulation of relational databases. In the context of Splitwave, Prisma plays a crucial role in modeling the

PostgreSQL database, providing an abstraction layer that facilitates operations such as listing, filtering, insertion, updating, and deletion of data.

5.1.4 PostgreSQL

PostgreSQL is an open-source relational database management system, known for its reliability, robustness, and ability to handle large volumes of data. In Splitwave, PostgreSQL is used as the primary database, storing crucial geophysical information for analysis and decision-making.

5.2 Front-end: Technologies and Architecture

5.2.1 Astro

Astro is a JavaScript technology that allows the development of websites with any front-end technology or framework. It offers a modular and flexible approach to building responsive and intuitive user interfaces. In the context of Splitwave, Astro is employed to develop the system's front-end, providing a rich and interactive user experience.

5.2.2 Front-end and Back-end Integration

The architecture of Splitwave allows seamless integration between the front-end and the back-end, ensuring efficient and secure communication between the different system components. When a user interacts with the user interface, such as accessing a page or submitting a form, the front-end sends requests to the API server, which then processes these requests and interacts with the PostgreSQL database to retrieve or update the necessary data. This asynchronous communication approach allows for a smooth and responsive user experience, regardless of the complexity of the operations performed.



Figure 6 – Data Viewing Page: Users can search for data by station name in the white search tab on the right. To search by author, the white search tab on the left is available. To view a complete list of the studies used, users can click on the orange tab. Additionally, the page allows for the viewing of a map, which displays the location of the data. By clicking on each marker on the map, corresponding information for each station will be displayed.

5.3 Hosting and Infrastructure

5.3.1 Vercel and Google Cloud Run

The Splitwave front-end is hosted on the Vercel platform, which offers a scalable and reliable infrastructure for deploying web applications. On the other hand, the back-end server, built with Node.js and Hono, is hosted on Google Cloud Run, which provides a flexible and managed environment for running containers at scale. This distributed hosting approach ensures high availability and optimized performance for the Splitwave framework.

5.3.2 PostgreSQL Database on Amazon Web Services

The PostgreSQL database used by Splitwave is hosted on the Amazon Web Services (AWS) Realtime Database Service (RDS), a reliable and secure platform for storing and managing data. RDS offers advanced scalability, security, and disaster recovery features, ensuring the integrity and availability of the essential geophysical data for exploration.

6 CONCLUSIONS

In this work, new XK(K)S parameters for the Amazonian Craton, southeastern, and central-western regions of Brazil were presented, along with updated maps. The extensive analysis conducted sheds light on the ongoing exploration of shear wave splitting in the upper mantle within Brazilian territory. Despite significant progress, many areas remain unexplored, and the data collected in this study play a crucial role in enhancing Brazil's understanding of anisotropy. Furthermore, the reanalysis of stations previously examined by other studies has significantly enriched the updated datasets, contributing to a deeper comprehension of shear wave splitting.

The discourse surrounding observed upper mantle anisotropy in Brazil encompasses a spectrum of theories regarding its genesis. While some works, exemplified by [Conrad, Behn and Silver \(2007\)](#), attribute observed polarization directions to the influence of asthenospheric flow on olivine, others propose alternative hypotheses suggesting that polarization directions may stem from regions subjected to significant shearing during historical periods, resulting in "frozen" or "fossilized" anisotropy.

The comprehensive analysis of over 70 stations across Brazil has provided diverse insights into the factors influencing polarization directions. Notably, in the southern region of the São Francisco Craton and the southeastern Tocantins Fold Belt, observed values tend to align with a NW-SE orientation, consistent with previous findings. However, contrasting interpretations by [Assumpção et al. \(2006\)](#) suggest different alignments parallel to the Goiânia fold, resulting from the collision of the Paranapanema cratonic block beneath the Paraná Basin and the São Francisco Craton. In the northern segment of the Tocantins Fold Belt, polarization directions trend towards a WSW-ENE orientation.

Additionally, [Melo \(2018\)](#) asserts that the observed parameters in southeastern Brazil, particularly in the São Francisco Craton, are more closely tied to the asthenospheric flow model, with minimal influence from geological structures. The Pantanal and Paraná Basins exhibit values that align with the absolute plate motion. In the Chaco-Paraná Basin, polarization direction values rotate to NW-SE, further confirming the influence of asthenospheric flow in the region.

In the Amazonian region, particularly in the Amazon Basin, the predominant orientation of the polarization directions tends towards WSW-ENE. This orientation aligns with the absolute plate motion (HS3-NUVEL1A), suggesting a correlation between regional tectonic dynamics and anisotropic behavior. In the center of the Central Brazilian Shield, a study by [Rosa-Costa et al. \(2006\)](#) identified the Moho thickness, indicating a possible cratonic root. It is observed that both the polarization directions and [Conrad, Behn and Silver \(2007\)](#) numerical model of mantle flow deviate in regions with greater Moho depth (approximately 60 km). In the northeastern portion of the Central Brazilian Shield, [Andrade and Assumpção \(2008\)](#) detected S-wave velocity anomalies at a depth of 150 km, indicating a cratonic root. The observed parameters near this region seem to undergo a deflection, suggesting that the polarization directions are influenced by asthenospheric flow. To confirm the deflection of fast polarization directions around the cratonic core, more stations need to be installed in the area inferred to contain the Amazonian cratonic root. Due to the limited number of stations, assertions regarding the deflection around the cratonic core remain inconclusive.

The observed delay times in the cratonic regions are short, with an average below 0.8 seconds ([Table 1](#)). The average polarization direction in the craton is 99.70° , tending towards ENE-WSW, consistent with results from other works ([Melo et al. \(2018\)](#); [Assumpção et al. \(2006\)](#); [Assumpção et al. \(2011\)](#)). The average delay time in the Tocantins Province exceeds 1 second ([Figure 4](#)), indicating that the anisotropic

source may differ from those in other regions. Areas known for their fold belts, such as the Ribeira Belt and the Tocantins Province, exhibit high delay times. These areas are characterized by fold belts resulting from the collision of blocks during the formation of Gondwana. A closer look at both the polarization directions and the average delay times shows values consistent with the presence of fossilized anisotropy. The collision of blocks results in significant shear stress, which can create a thick anisotropic layer. Overall, the fold belts exhibit average polarization direction values of 87.30° and a delay time of 1.15 seconds.

On the other hand, the study conducted by [Melo et al. \(2018\)](#) suggests that in southeastern Brazil, the influence is related to mantle flow. The values observed in the basins are consistent, with average polarization directions close to 93.03° ([Table 1](#)) and average delay times around 0.8 second ([Table 1](#)). Moreover, the parameters observed in the basins tend to align mostly with the direction of absolute plate motion (ENE-WSW), which aligns with the observations made by [Melo et al. \(2018\)](#) in their study

While the northeastern region shows results with low signal-to-noise ratio limitations and data categorization issues, observations underscore a propensity for polarization directions to align with geological structures. The parameters obtained closely align with the numerical model proposed by [Conrad, Behn and Silver \(2007\)](#).

In summary, the cratonic regions exhibit average polarization directions of 99.70° and delay times of 0.72 seconds. Basins show average values of 93.03° and 0.83 seconds, with directions oriented towards ENE-WSW corresponding to the Absolute Plate Motion (APM). Fold belts average 87.30° and 1.15 seconds. The higher delay times in fold belts are characteristic, indicating distinct sources of anisotropy in these regions. It is noteworthy that polarization directions vary across these regions, influencing the orientations of ϕ parameters. This variability underscores the complexity and regional differences in anisotropic seismic.

BIBLIOGRAPHY

- Abramson, E. H. et al. The elastic constants of san carlos olivine to 17 gpa. *Journal of Geophysical Research: Solid Earth*, v. 102, p. 12253–12263, 6 1997. ISSN 0148-0227. Quoted on page 14.
- Anderson, D. L. Elastic wave propagation in layered anisotropic media. *Journal of Geophysical Research*, Wiley Online Library, v. 66, n. 9, p. 2953–2963, 1961. Quoted on page 14.
- Andrade, M. G. d.; Assumpção, M. S. d. Anisotropia sísmica do manto superior na américa do sul com a divisão de ondas sks. 2008. Quoted 5 times on pages 14, 33, 35, 36, and 40.
- Andrade, M. G. de. Anisotropia sísmica do manto superior na américa do sul com a divisão de ondas sks. 2008. Quoted on page 14.
- Assumpção, M. et al. Upper-mantle seismic anisotropy from sks splitting in the south american stable platform: a test of asthenospheric flow models beneath the lithosphere. *Lithosphere*, Geological Society of America, v. 3, n. 2, p. 173–180, 2011. Quoted 3 times on pages 33, 35, and 40.
- Assumpção, M. et al. Upper mantle anisotropy in se and central brazil from sks splitting: evidence of asthenospheric flow around a cratonic keel. *Earth and Planetary Science Letters*, Elsevier, v. 250, n. 1-2, p. 224–240, 2006. Quoted 3 times on pages 33, 35, and 40.
- Bystricky, M. et al. High shear strain of olivine aggregates: Rheological and seismic consequences. *Science*, American Association for the Advancement of Science, v. 290, n. 5496, p. 1564–1567, 2000. Quoted on page 14.
- Conrad, C. P.; Behn, M. D.; Silver, P. G. Global mantle flow and the development of seismic anisotropy: Differences between the oceanic and continental upper mantle. *Journal of Geophysical Research: Solid Earth*, Wiley Online Library, v. 112, n. B7, 2007. Quoted 4 times on pages 33, 34, 40, and 41.
- Cordani, U. G. et al. The new tectonic map of south america (2016) at 1: 5 000 000 scale. In: *35th International Geological Congress*. 2016. Quoted 3 times on pages 9, 35, and 36.
- Demouchy, S.; Wang, Q.; Tommasi, A. Deforming the upper mantle—olivine mechanical properties and anisotropy. *Elements*, Mineralogical Society of America, v. 19, n. 3, p. 151–157, 2023. Quoted 3 times on pages 13, 14, and 15.
- Efron, B. The 1977 rietz lecture. *The annals of Statistics*, v. 7, n. 1, p. 1–26, 1979. Quoted on page 18.
- Feng, M.; Lee, S. Van der; Assumpção, M. Upper mantle structure of south america from joint inversion of waveforms and fundamental mode group velocities of rayleigh waves. *Journal of Geophysical Research: Solid Earth*, Wiley Online Library, v. 112, n. B4, 2007. Quoted on page 33.
- James, D. E.; Assumpção, M. Tectonic implications of s-wave anisotropy beneath se brazil. *Geophysical Journal International*, Blackwell Publishing Ltd Oxford, UK, v. 126, n. 1, p. 1–10, 1996. Quoted 4 times on pages 33, 34, 35, and 36.
- Link, F.; Reiss, M. C.; Rumpker, G. An automatized xks-splitting procedure for large data sets: Extension package for splitracer and application to the usarray. *Computers & Geosciences*, Elsevier, v. 158, p. 104961, 2022. Quoted on page 18.
- Melo, B. C. d. *Mantle Anisotropy and Asthenospheric Flow Around Cratons in SE South America*. Tese (Doutorado) — Universidade de São Paulo, 2018. Quoted on page 40.
- Melo, B. C. de et al. Mantle anisotropy and asthenospheric flow around cratons in southeastern south america. *Geophysical Journal International*, v. 215, 2018. ISSN 1365246X. Quoted 7 times on pages 9, 33, 34, 35, 36, 40, and 41.
- Nascimento, A. V. et al. Unraveling precambrian cratonic roots beneath south america: A contribution from surface wave tomography. *Tectonophysics*, v. 883, p. 230392, 2024. ISSN 0040-1951. Available on: <<https://www.sciencedirect.com/science/article/pii/S004019512400194X>>. Quoted on page 33.

Nicolas, A. Why fast polarization directions of SKS seismic waves are parallel to mountain belts. *Physics of the earth and planetary interiors*, Elsevier, v. 78, n. 3-4, p. 337–342, 1993. Quoted on page 14.

Reiss, M. C.; Rumpker, G. Splitracer: Matlab code and gui for semiautomated analysis and interpretation of teleseismic shear-wave splitting. *Seismological Research Letters*, Seismological Society of America, v. 88, n. 2A, p. 392–409, 2017. Quoted 3 times on pages 16, 17, and 18.

Rosa-Costa, L. T. d. et al. Geocronologia 207pb/206pb, sm-nd, u-th-pb e 40ar-39ar do segmento sudeste do escudo das guianas: Evolução crustal e termocronologia do evento transamazônico. Universidade Federal do Pará, 2006. Quoted 2 times on pages 33 and 40.

Russo, R.; Silver, P. Trench-parallel flow beneath the Nazca plate from seismic anisotropy. *Science*, American Association for the Advancement of Science, v. 263, n. 5150, p. 1105–1111, 1994. Quoted on page 14.

Silver, P. G. Seismic anisotropy beneath the continents: Probing the depths of geology. *Annual review of earth and planetary sciences*, Annual Reviews 4139 El Camino Way, PO Box 10139, Palo Alto, CA 94303-0139, USA, v. 24, n. 1, p. 385–432, 1996. Quoted on page 13.

Silver, P. G.; Chan, W. W. Shear wave splitting and subcontinental mantle deformation. *Journal of Geophysical Research: Solid Earth*, Wiley Online Library, v. 96, n. B10, p. 16429–16454, 1991. Quoted 4 times on pages 14, 16, 17, and 18.

Sá, L. A. de et al. *SplitWave - Database*. Zenodo, 2024. Available on: <<https://doi.org/10.5281/zenodo.10988278>>. Quoted on page 13.

Walsh, E.; Arnold, R.; Savage, M. Silver and Chan revisited. *Journal of Geophysical Research: Solid Earth*, Wiley Online Library, v. 118, n. 10, p. 5500–5515, 2013. Quoted 2 times on pages 17 and 18.

Wessel, P. et al. The generic mapping tools version 6. *Geochemistry, Geophysics, Geosystems*, Wiley Online Library, v. 20, n. 11, p. 5556–5564, 2019. Quoted on page 5.

Wüstefeld, A. et al. Splitlab: A shear-wave splitting environment in Matlab. *Computers & Geosciences*, Elsevier, v. 34, n. 5, p. 515–528, 2008. Quoted on page 18.

Appendix

APPENDIX A – BOOSTRAPPING

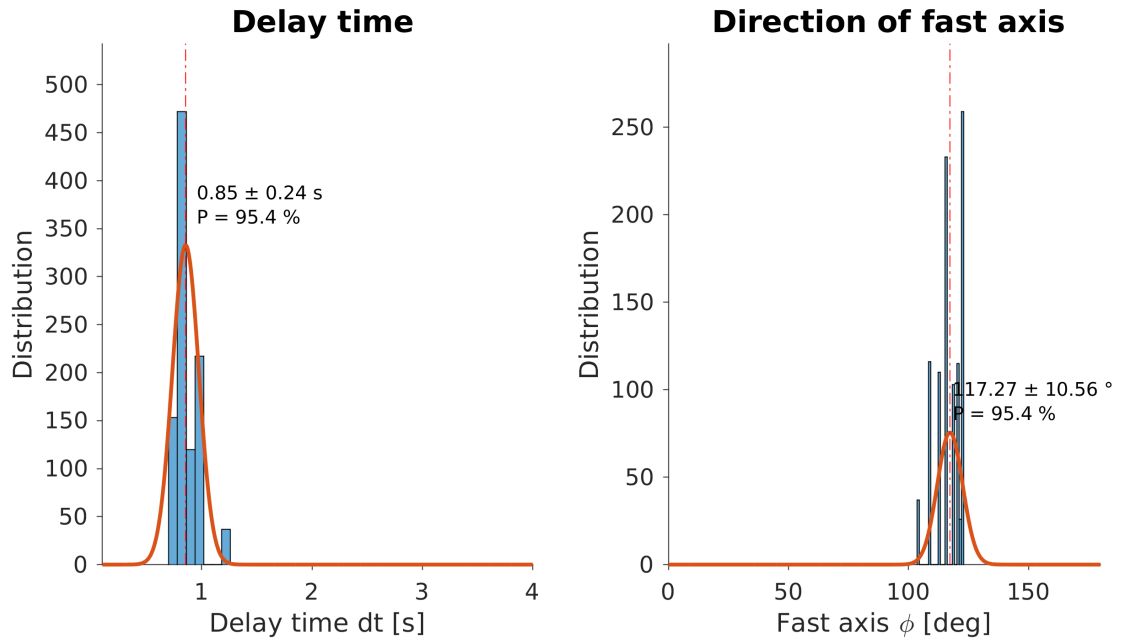


Figure A.1 – Anisotropic parameters obtained through the bootstrap technique at station AQDB, displaying the distribution of observed values (blue bars), the normal distribution curve (orange line), and the estimated value for the parameters (dashed orange vertical line).

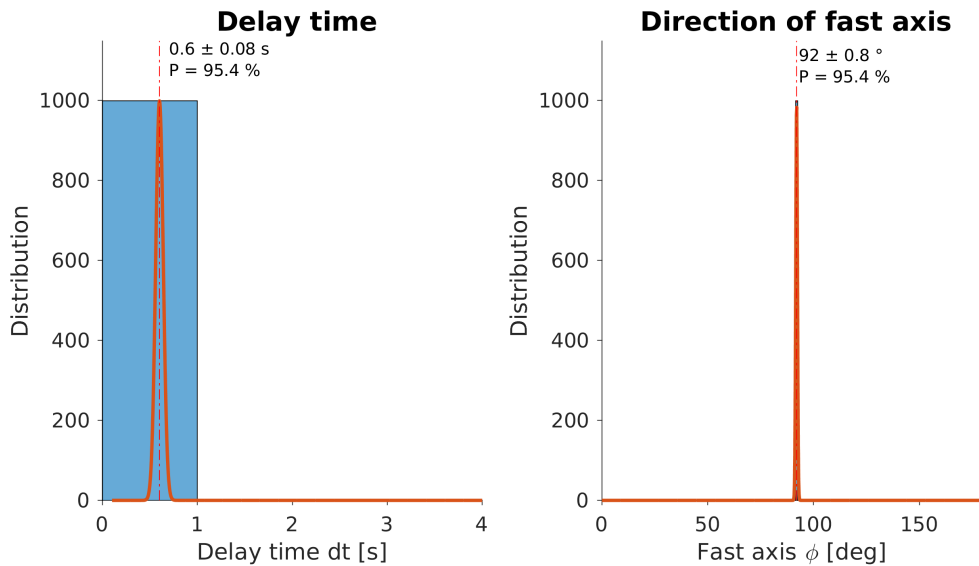


Figure A.2 – Anisotropic parameters obtained through the bootstrap technique at station BEB11, displaying the distribution of observed values (blue bars), the normal distribution curve (orange line), and the estimated value for the parameters (dashed orange vertical line).

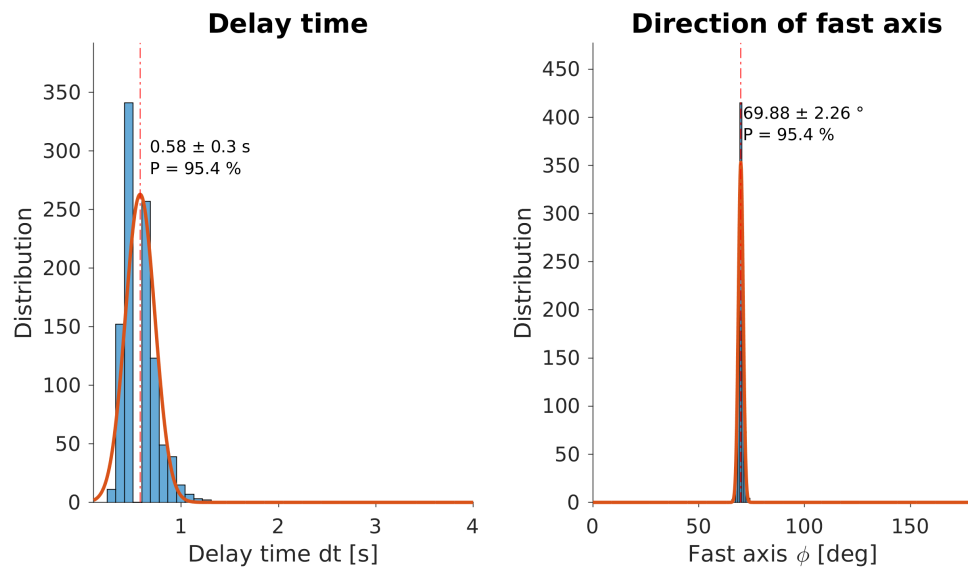


Figure A.3 – Anisotropic parameters obtained through the bootstrap technique at station BOAV, displaying the distribution of observed values (blue bars), the normal distribution curve (orange line), and the estimated value for the parameters (dashed orange vertical line).

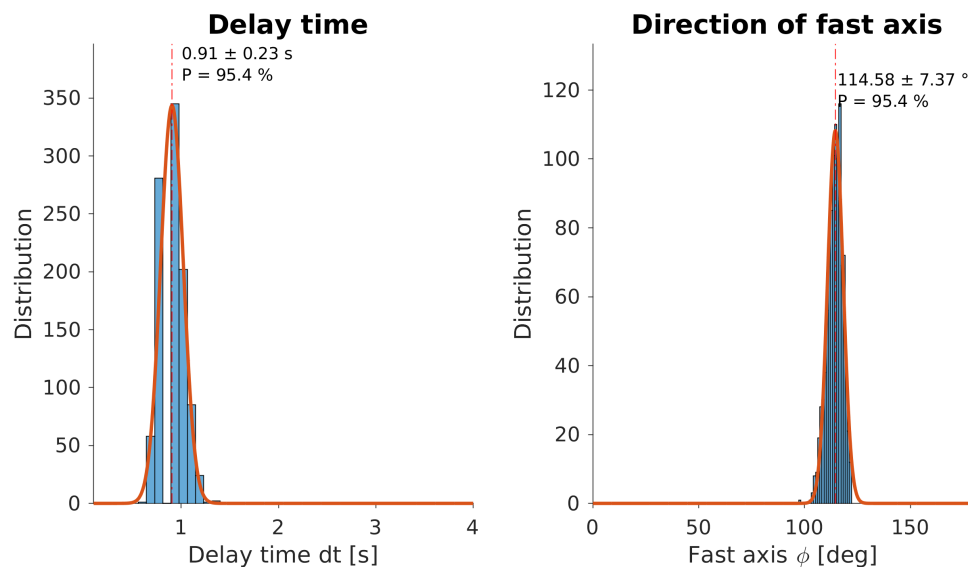


Figure A.4 – Anisotropic parameters obtained through the bootstrap technique at station BSCB, displaying the distribution of observed values (blue bars), the normal distribution curve (orange line), and the estimated value for the parameters (dashed orange vertical line).

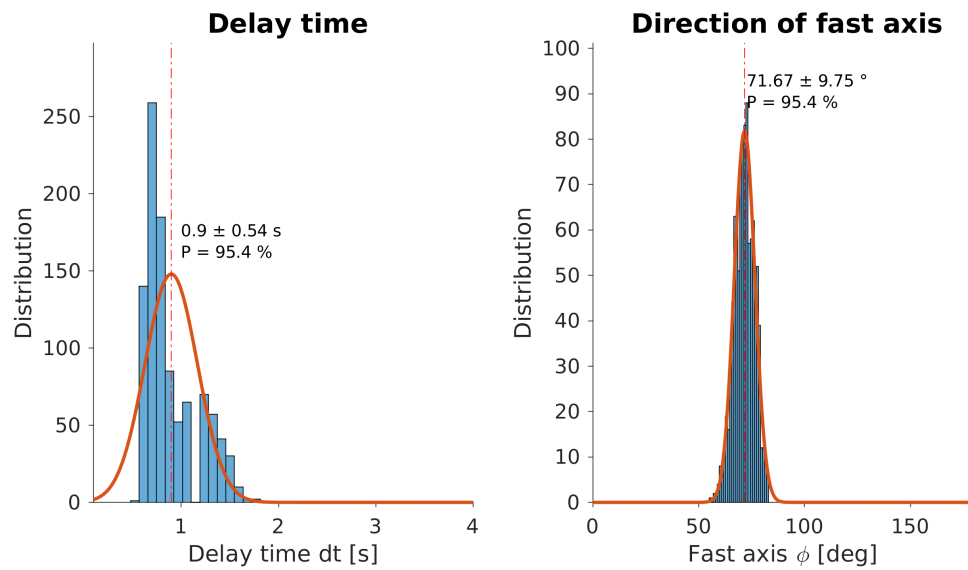


Figure A.5 – Anisotropic parameters obtained through the bootstrap technique at station BSFB, displaying the distribution of observed values (blue bars), the normal distribution curve (orange line), and the estimated value for the parameters (dashed orange vertical line).

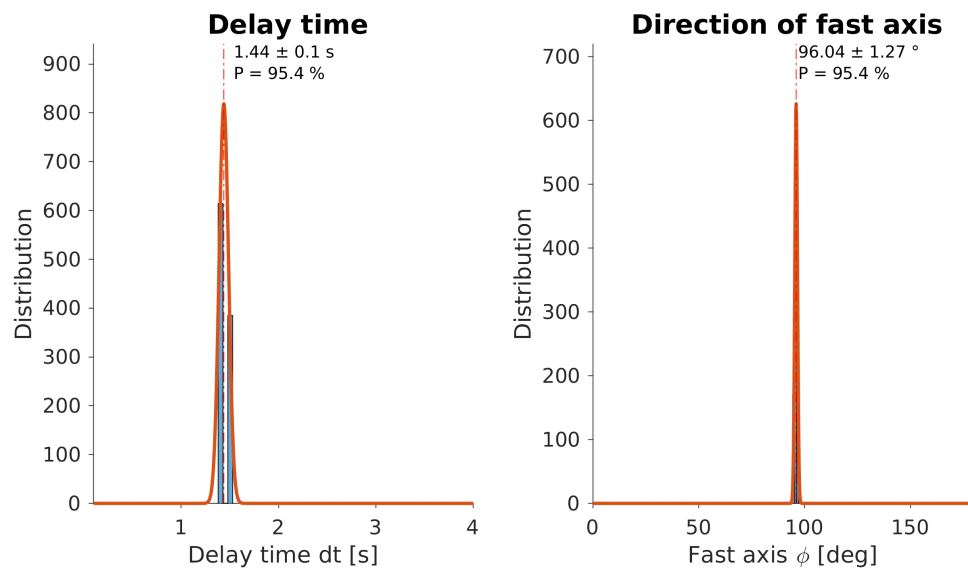


Figure A.6 – Anisotropic parameters obtained through the bootstrap technique at station CPSB, displaying the distribution of observed values (blue bars), the normal distribution curve (orange line), and the estimated value for the parameters (dashed orange vertical line).

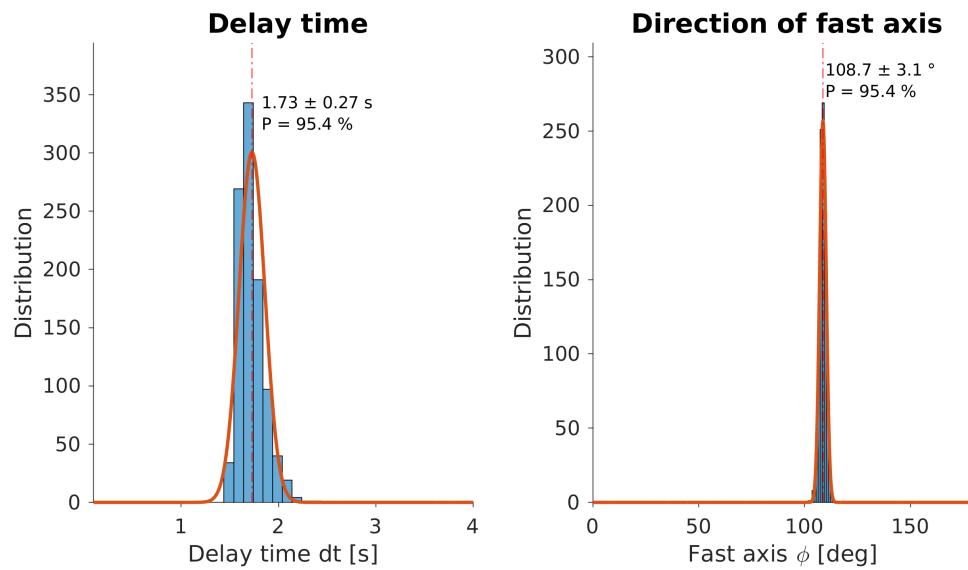


Figure A.7 – Anisotropic parameters obtained through the bootstrap technique at station ESAR, displaying the distribution of observed values (blue bars), the normal distribution curve (orange line), and the estimated value for the parameters (dashed orange vertical line).

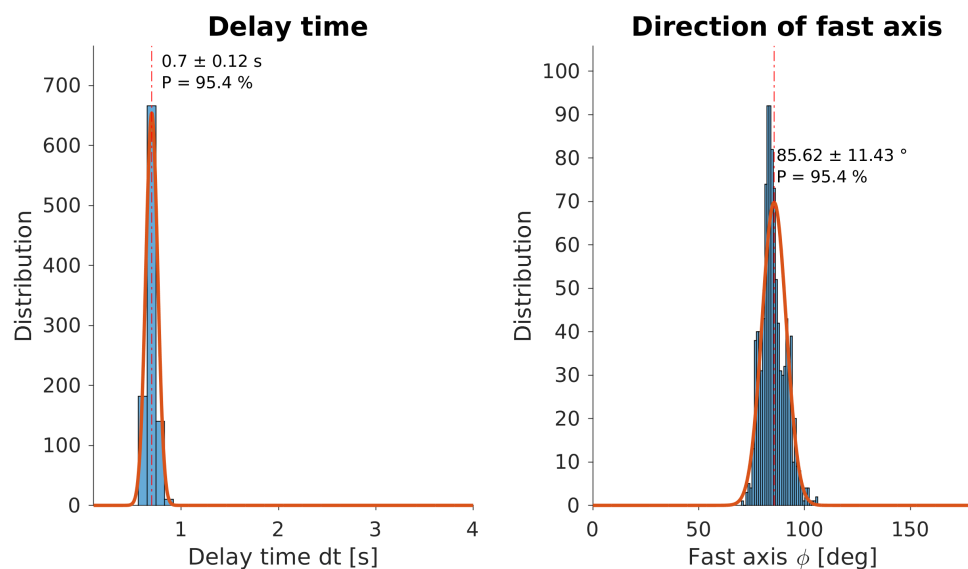


Figure A.8 – Anisotropic parameters obtained through the bootstrap technique at station IPMB, displaying the distribution of observed values (blue bars), the normal distribution curve (orange line), and the estimated value for the parameters (dashed orange vertical line).

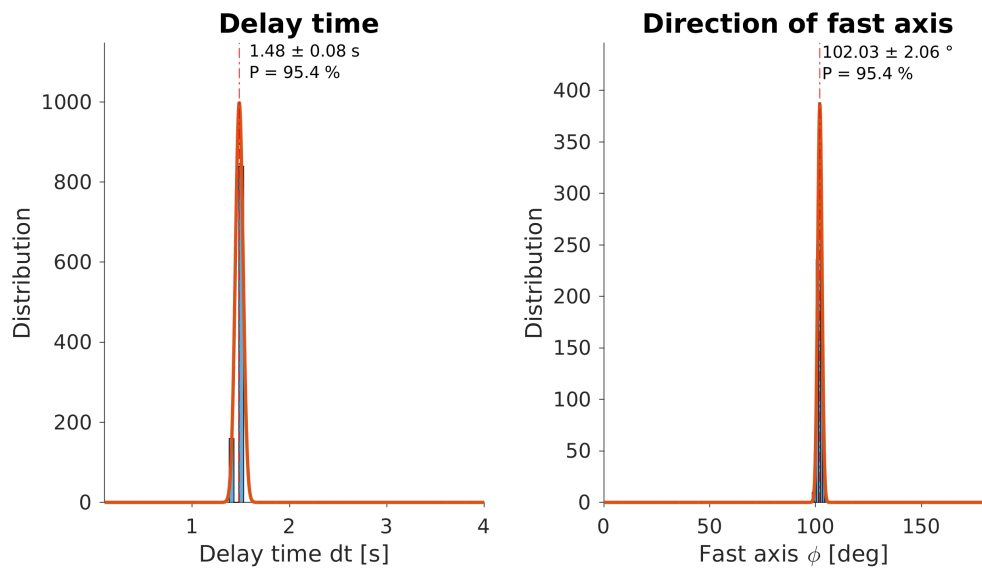


Figure A.9 – Anisotropic parameters obtained through the bootstrap technique at station ITAB, displaying the distribution of observed values (blue bars), the normal distribution curve (orange line), and the estimated value for the parameters (dashed orange vertical line).

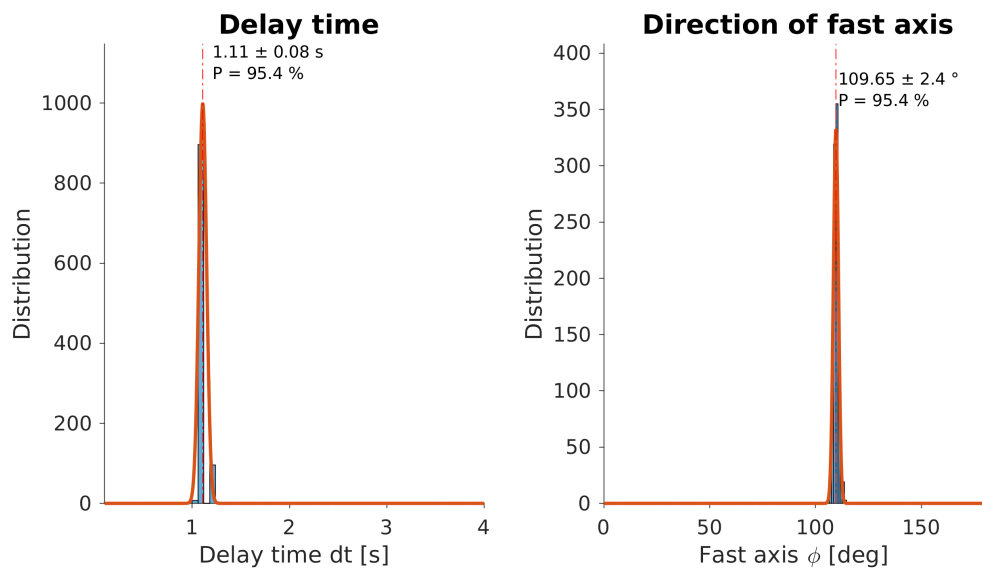


Figure A.10 – Anisotropic parameters obtained through the bootstrap technique at station ITQB, displaying the distribution of observed values (blue bars), the normal distribution curve (orange line), and the estimated value for the parameters (dashed orange vertical line).

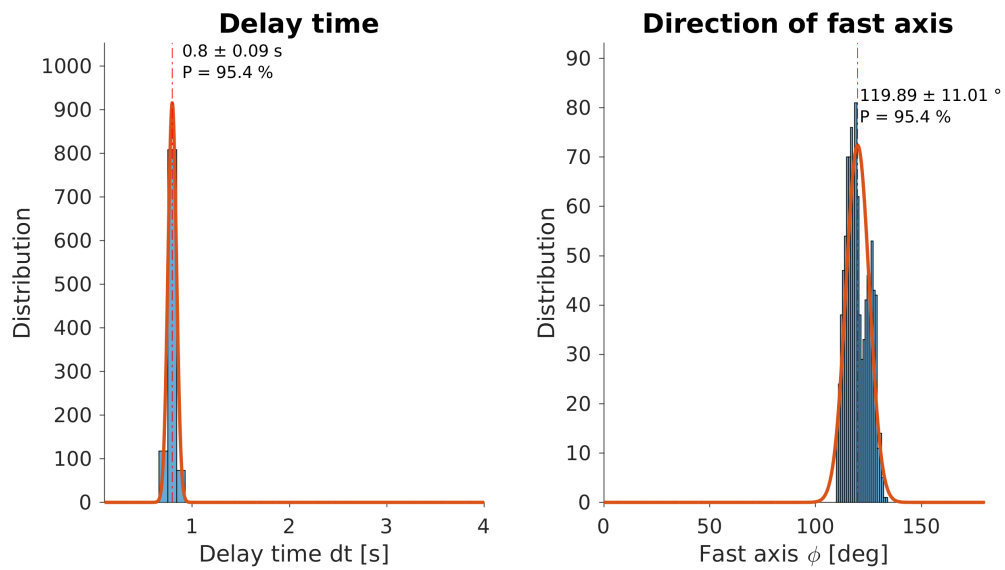


Figure A.11 – Anisotropic parameters obtained through the bootstrap technique at station MACA, displaying the distribution of observed values (blue bars), the normal distribution curve (orange line), and the estimated value for the parameters (dashed orange vertical line).

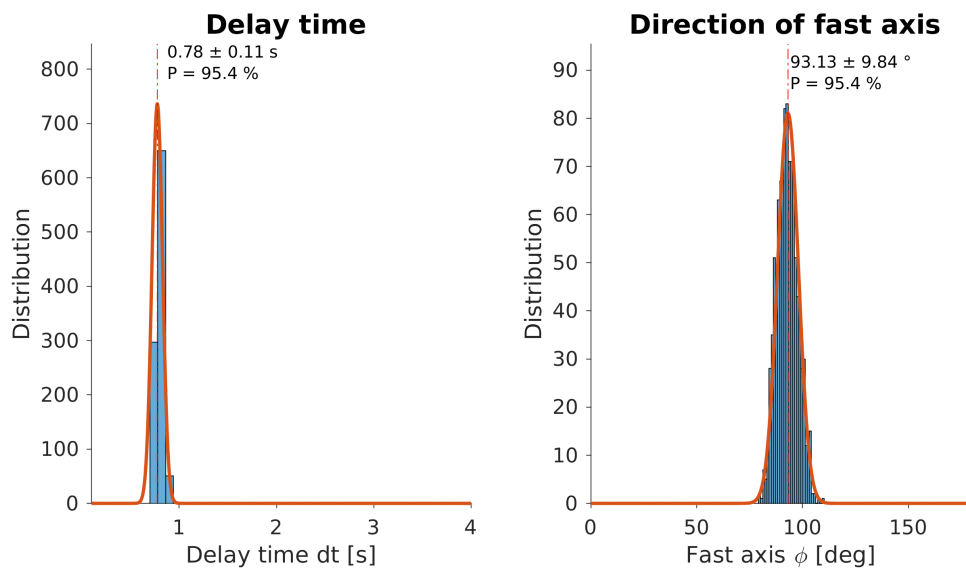


Figure A.12 – Anisotropic parameters obtained through the bootstrap technique at station MALB, displaying the distribution of observed values (blue bars), the normal distribution curve (orange line), and the estimated value for the parameters (dashed orange vertical line).

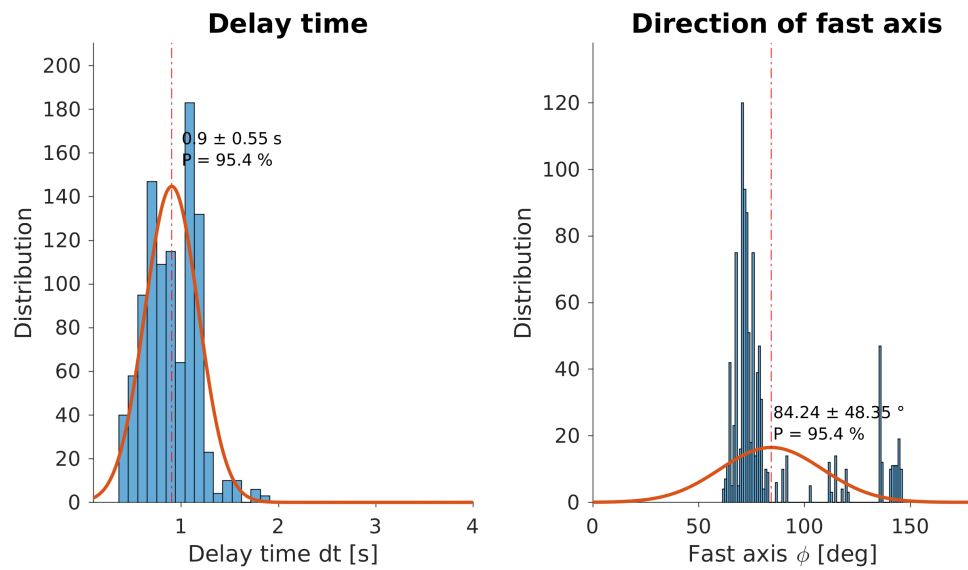


Figure A.13 – Anisotropic parameters obtained through the bootstrap technique at station MCPB, displaying the distribution of observed values (blue bars), the normal distribution curve (orange line), and the estimated value for the parameters (dashed orange vertical line).

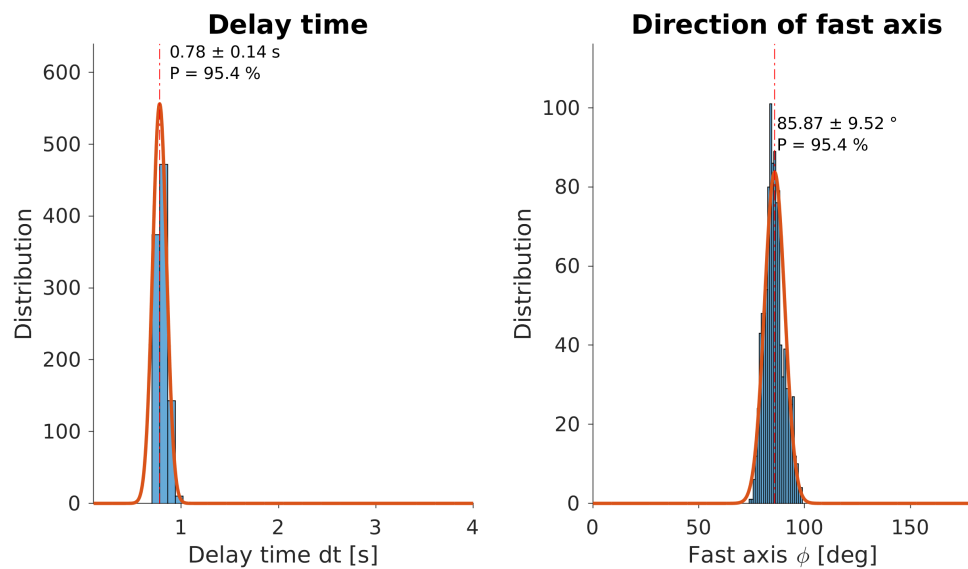


Figure A.14 – Anisotropic parameters obtained through the bootstrap technique at station NPGb, displaying the distribution of observed values (blue bars), the normal distribution curve (orange line), and the estimated value for the parameters (dashed orange vertical line).

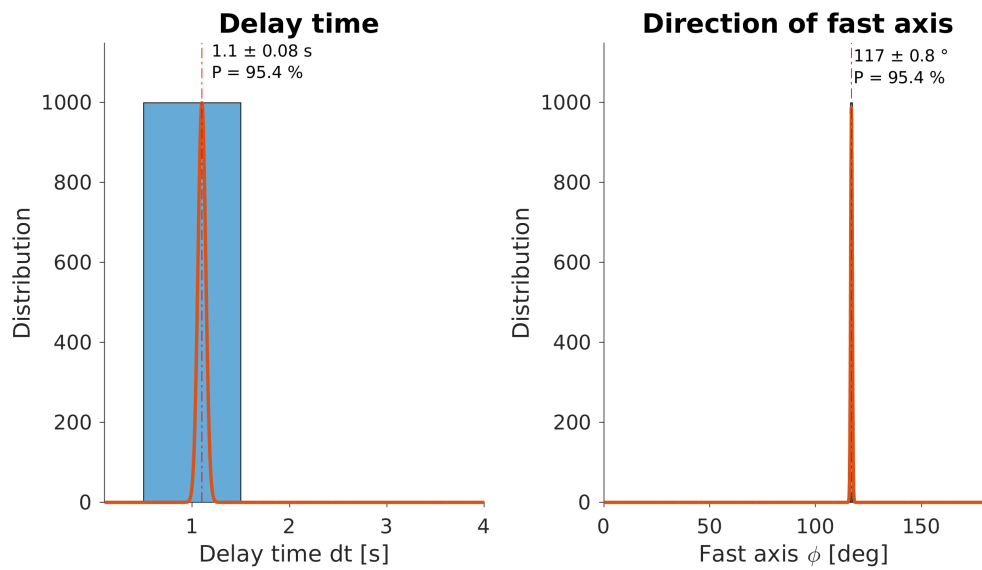


Figure A.15 – Anisotropic parameters obtained through the bootstrap technique at station PARB, displaying the distribution of observed values (blue bars), the normal distribution curve (orange line), and the estimated value for the parameters (dashed orange vertical line).

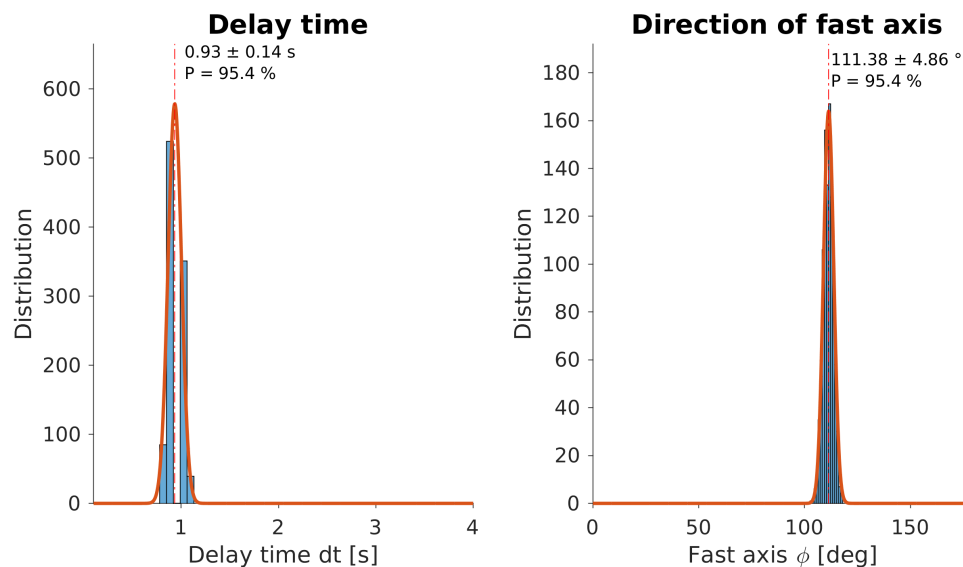


Figure A.16 – Anisotropic parameters obtained through the bootstrap technique at station PDRB, displaying the distribution of observed values (blue bars), the normal distribution curve (orange line), and the estimated value for the parameters (dashed orange vertical line).

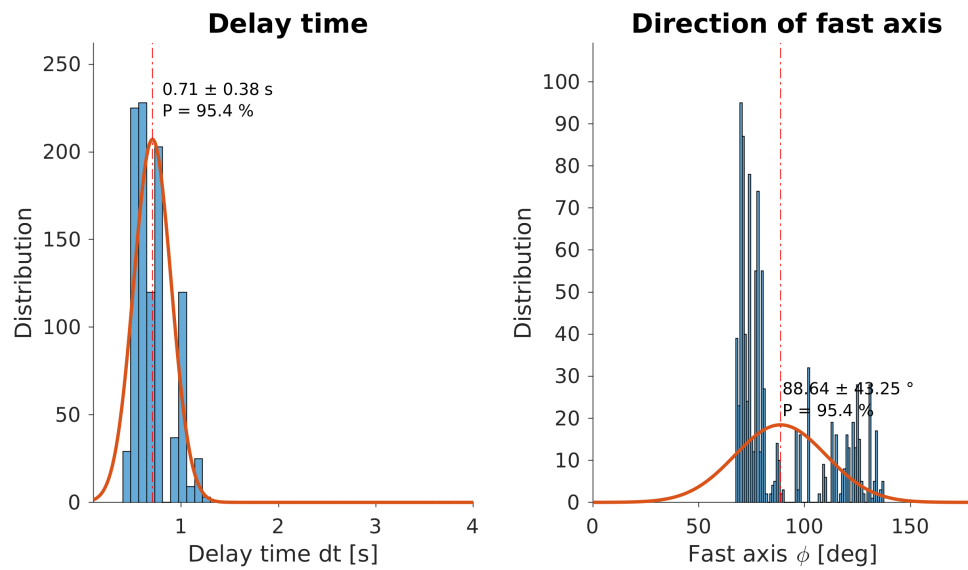


Figure A.17 – Anisotropic parameters obtained through the bootstrap technique at station PEXB, displaying the distribution of observed values (blue bars), the normal distribution curve (orange line), and the estimated value for the parameters (dashed orange vertical line).

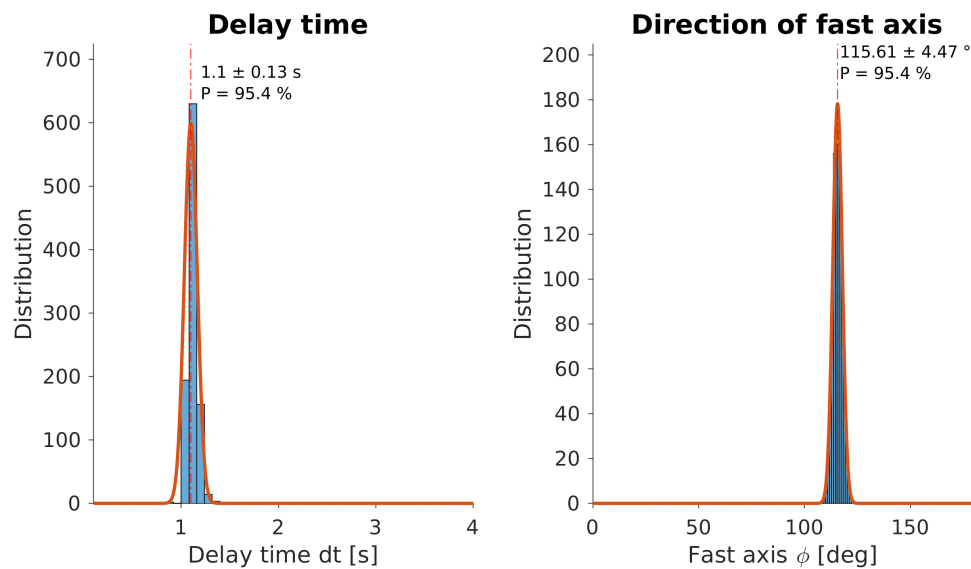


Figure A.18 – Anisotropic parameters obtained through the bootstrap technique at station PMNB, displaying the distribution of observed values (blue bars), the normal distribution curve (orange line), and the estimated value for the parameters (dashed orange vertical line).

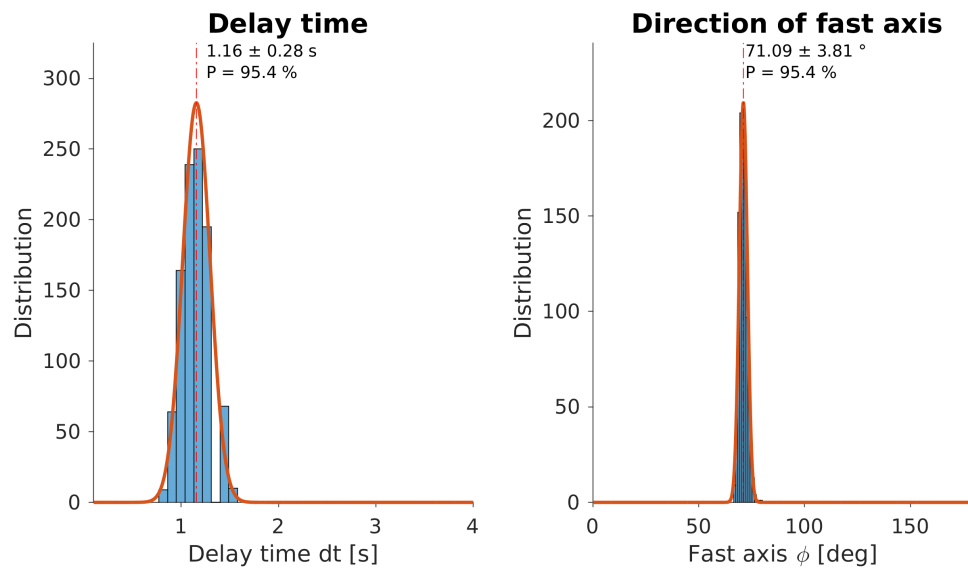


Figure A.19 – Anisotropic parameters obtained through the bootstrap technique at station PRPB, displaying the distribution of observed values (blue bars), the normal distribution curve (orange line), and the estimated value for the parameters (dashed orange vertical line).

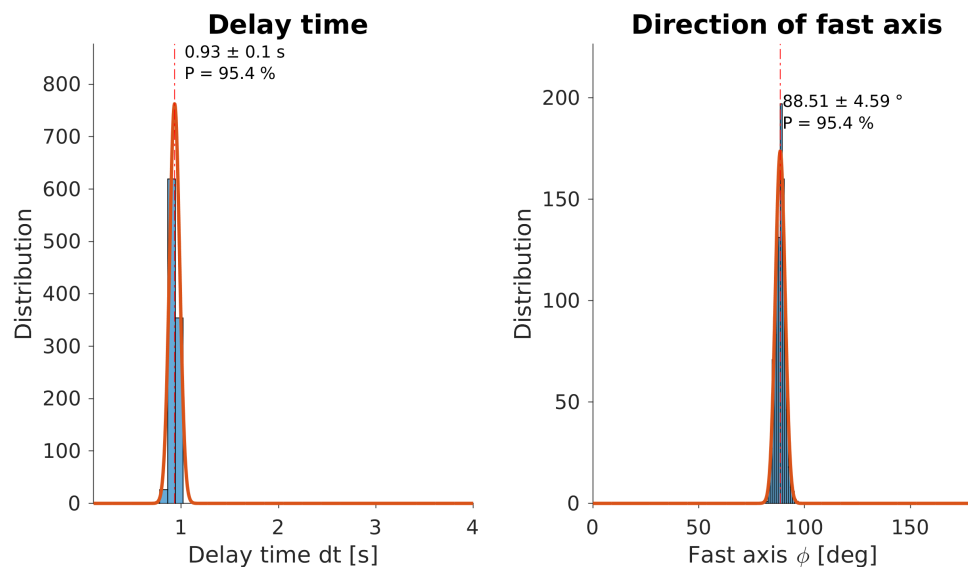


Figure A.20 – Anisotropic parameters obtained through the bootstrap technique at station PTLB, displaying the distribution of observed values (blue bars), the normal distribution curve (orange line), and the estimated value for the parameters (dashed orange vertical line).

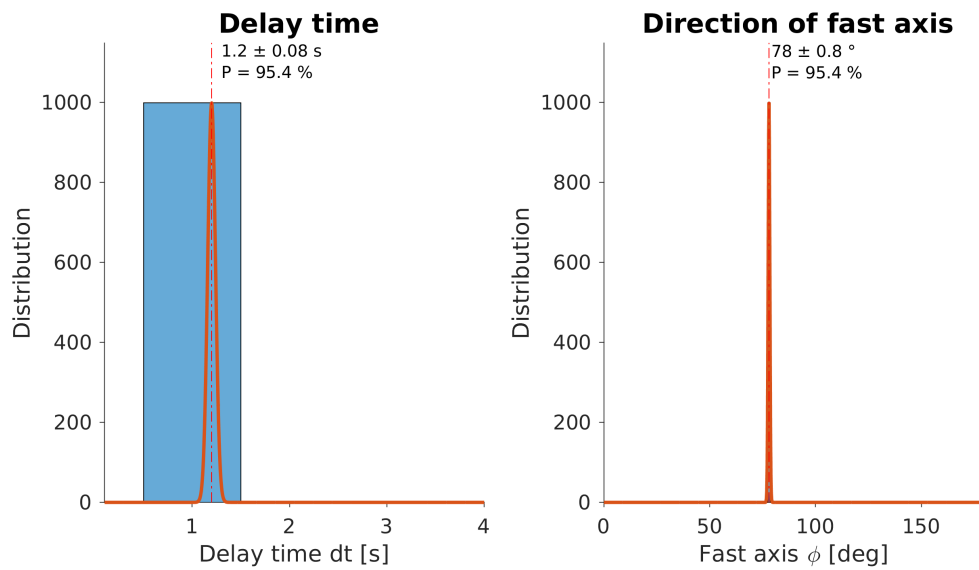


Figure A.21 – Anisotropic parameters obtained through the bootstrap technique at station ROIB, displaying the distribution of observed values (blue bars), the normal distribution curve (orange line), and the estimated value for the parameters (dashed orange vertical line).

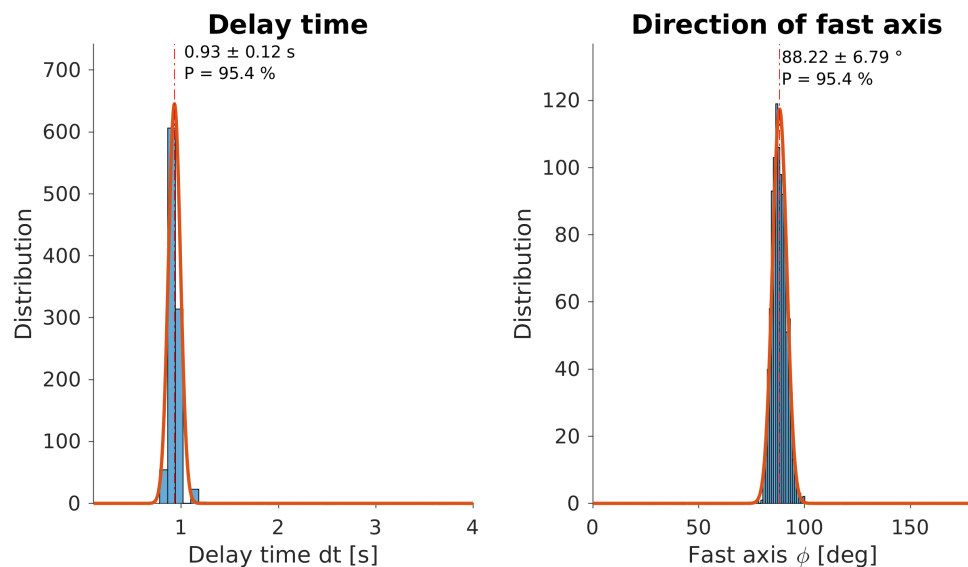


Figure A.22 – Anisotropic parameters obtained through the bootstrap technique at station ROSB, displaying the distribution of observed values (blue bars), the normal distribution curve (orange line), and the estimated value for the parameters (dashed orange vertical line).

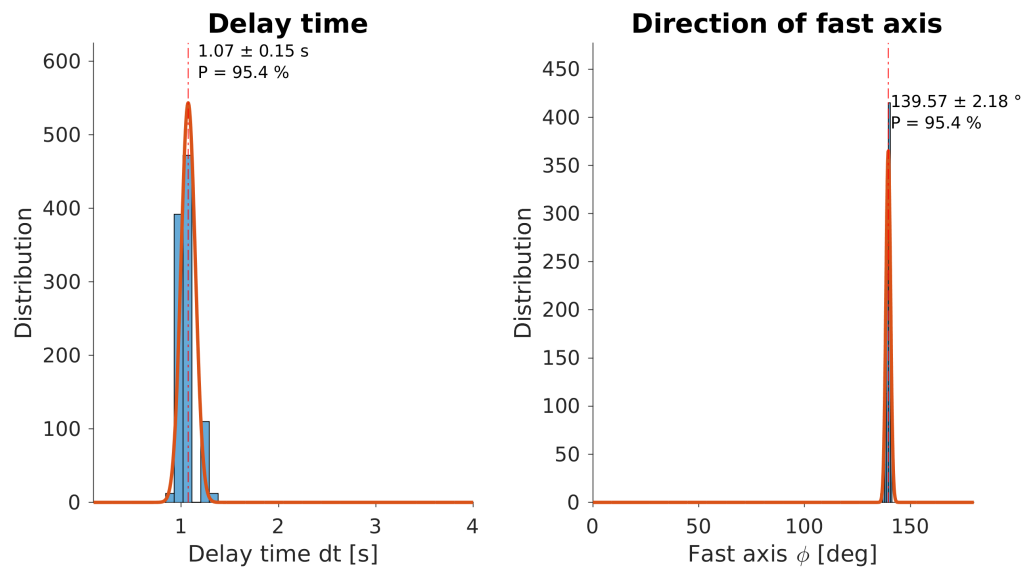


Figure A.23 – Anisotropic parameters obtained through the bootstrap technique at station SDBA, displaying the distribution of observed values (blue bars), the normal distribution curve (orange line), and the estimated value for the parameters (dashed orange vertical line).

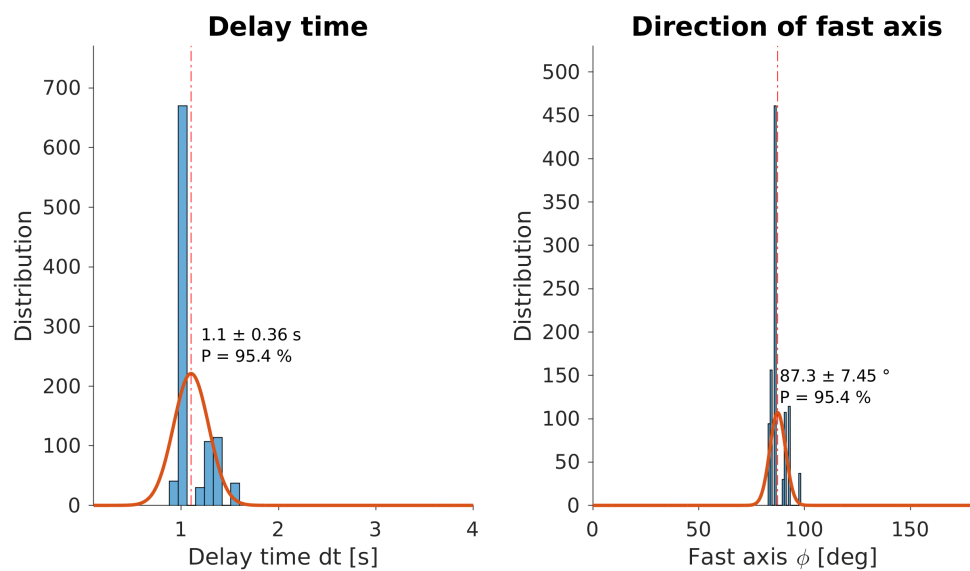


Figure A.24 – Anisotropic parameters obtained through the bootstrap technique at station SICB, displaying the distribution of observed values (blue bars), the normal distribution curve (orange line), and the estimated value for the parameters (dashed orange vertical line).

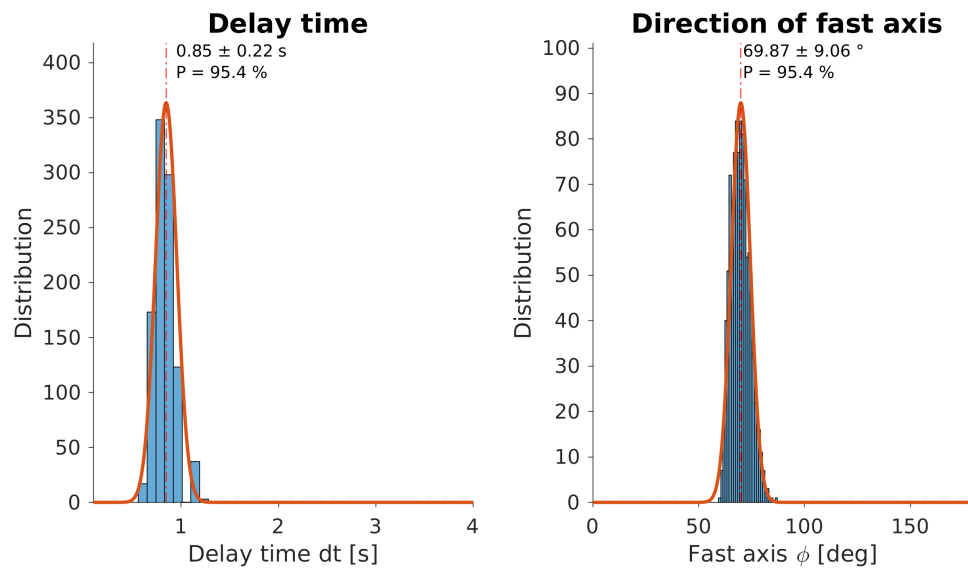


Figure A.25 – Anisotropic parameters obtained through the bootstrap technique at station SJMB, displaying the distribution of observed values (blue bars), the normal distribution curve (orange line), and the estimated value for the parameters (dashed orange vertical line).

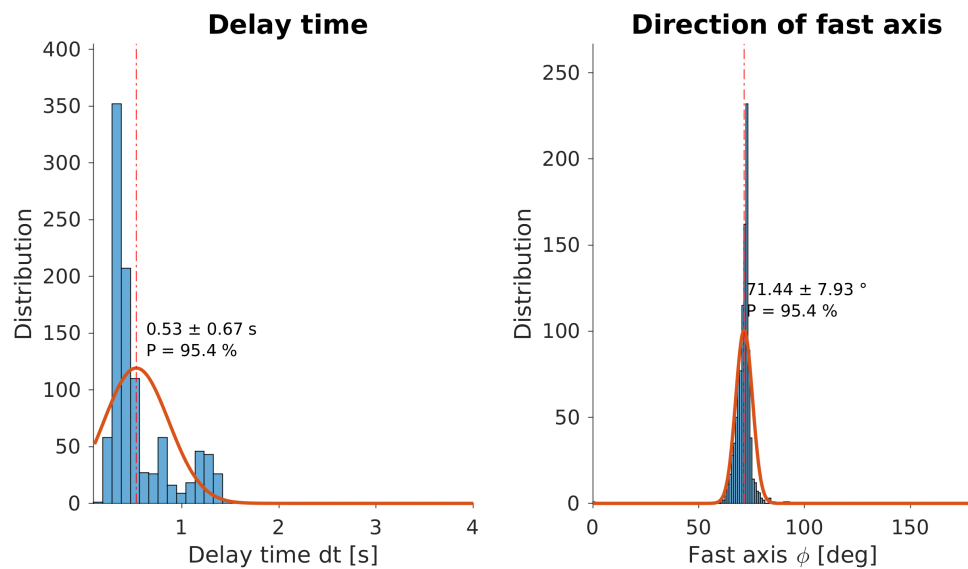


Figure A.26 – Anisotropic parameters obtained through the bootstrap technique at station TBTG, displaying the distribution of observed values (blue bars), the normal distribution curve (orange line), and the estimated value for the parameters (dashed orange vertical line).

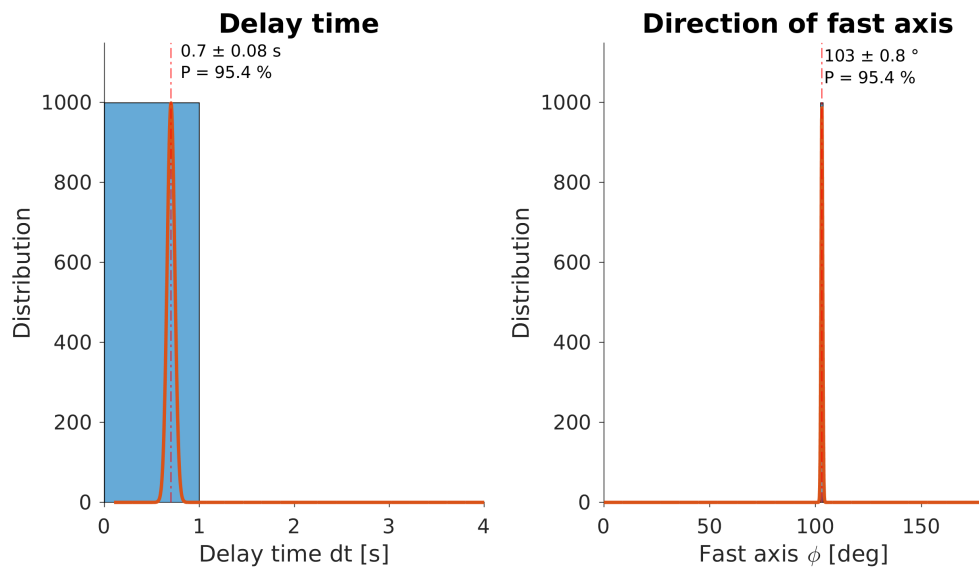


Figure A.27 – Anisotropic parameters obtained through the bootstrap technique at station TRIB, displaying the distribution of observed values (blue bars), the normal distribution curve (orange line), and the estimated value for the parameters (dashed orange vertical line).

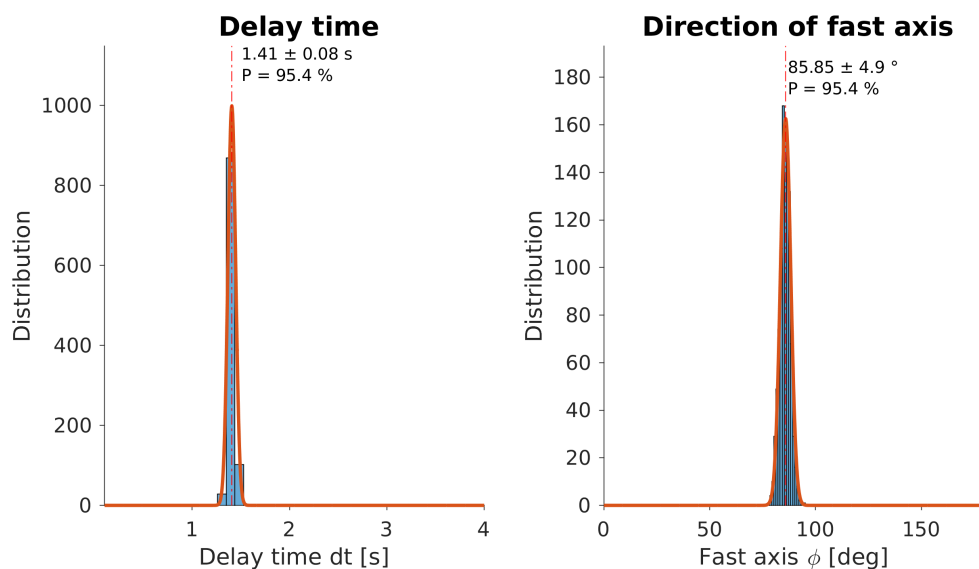


Figure A.28 – Anisotropic parameters obtained through the bootstrap technique at station VABB, displaying the distribution of observed values (blue bars), the normal distribution curve (orange line), and the estimated value for the parameters (dashed orange vertical line).

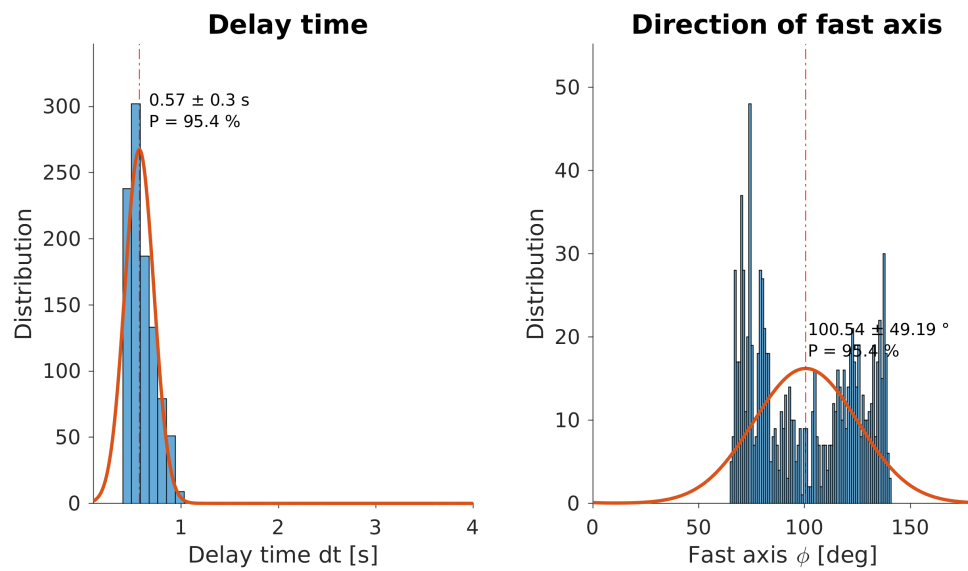


Figure A.29 – Anisotropic parameters obtained through the bootstrap technique at station VILB, displaying the distribution of observed values (blue bars), the normal distribution curve (orange line), and the estimated value for the parameters (dashed orange vertical line).